A&A 627, A116 (2019)
https://doi.org/10.1051/0004-6361/201935534

Astronomy & Astrophysics

The CARMENES search for exoplanets around M dwarfs

Detection of a mini-Neptune around LSPM J2116+0234 and refinement of orbital parameters of a super-Earth around GJ 686 (BD+18 3421)★

S. Lalitha[1,★★], D. Baroch[2,3,★★], J. C. Morales[2,3], V. M. Passegger[4], F. F. Bauer[5], C. Cardona Guillén[6,7], S. Dreizler[1], M. Oshagh[1], A. Reiners[1], I. Ribas[2,3], J. A. Caballero[8], A. Quirrenbach[9], P. J. Amado[5], V. J. S. Béjar[6,7], J. Colomé[2,3], M. Cortés-Contreras[8], D. Galadí-Enríquez[10], L. González-Cuesta[6,7], E. W. Guenther[11], H.-J. Hagen[4], T. Henning[12], E. Herrero[2,3], T.-O. Husser[1], S. V. Jeffers[1], A. Kaminski[9], M. Kürster[12], M. Lafarga[2,3], N. Lodieu[6,7], M. J. López-González[5], D. Montes[13], M. Perger[2,3], A. Rosich[2,3], E. Rodríguez[5], C. Rodríguez-López[5], J. H. M. M. Schmitt[4], L. Tal-Or[14,1], and M. Zechmeister[1]

(Affiliations can be found after the references)

Received 25 March 2019 / Accepted 14 May 2019

ABSTRACT

Although M dwarfs are known for high levels of stellar activity, they are ideal targets for the search of low-mass exoplanets with the radial velocity (RV) method. We report the discovery of a planetary-mass companion around LSPM J2116+0234 (M3.0 V) and confirm the existence of a planet orbiting GJ 686 (BD+18 3421; M1.0 V). The discovery of the planet around LSPM J2116+0234 is based on CARMENES RV observations in the visual and near-infrared channels. We confirm the planet orbiting around GJ 686 by analyzing the RV data spanning over two decades of observations from CARMENES VIS, HARPS-N, HARPS, and HIRES. We find planetary signals at 14.44 and 15.53 d in the RV data for LSPM J2116+0234 and GJ 686, respectively. Additionally, the RV, photometric time series, and various spectroscopic indicators show hints of variations of 42 d for LSPM J2116+0234 and 37 d for GJ 686, which we attribute to the stellar rotation periods. The orbital parameters of the planets are modeled with Keplerian fits together with correlated noise from the stellar activity. A mini-Neptune with a minimum mass of 11.8 $M_\oplus$ orbits LSPM J2116+0234 producing a RV semi-amplitude of 6.19 m s^{-1}, while a super-Earth of mass 6.6 $M_\oplus$ orbits GJ 686 and produces a RV semi-amplitude of 3.0 m s^{-1}. Both LSPM J2116+0234 and GJ 686 have planetary companions populating the regime of exoplanets with masses lower than 15 $M_\oplus$ and orbital periods <20 d.

Key words. stars: individual: LSPM J2116+0234 – stars: individual: GJ 686 – stars: low-mass – techniques: radial velocities – planetary systems – stars: activity

1. Introduction

Nearly 75% of the stellar population of our galaxy consists of M-type stars, making them the most common potential planetary hosts (Henry et al. 2006; Dressing & Charbonneau 2015; Gaidos et al. 2016). Since the discovery of the first exoplanet around a main-sequence star in 1995 (Mayor & Queloz 1995), an important goal has been the discovery and characterization of terrestrial planets located inside the habitable zone. M-dwarf stars are in the focus of ongoing surveys for habitable planets for two main reasons. Firstly, the induced radial velocity (RV) amplitude is inversely proportional to the mass of the star (Newton 1687), increasing the detection probability of lower mass planets around them (Marcy & Butler 1998; Udry et al. 2007; Bonfils et al. 2013). Secondly, as a consequence of the low luminosities of M dwarfs, their habitable zones are located closer to the host star with relatively shorter orbital periods.

The downside of surveying M-dwarf stars with high-resolution spectrographs is their high levels of magnetic activity. Large inhomogeneities such as dark spots and bright faculae are produced on the stellar surface owing to this activity, which in turn affects the spectral line profile and induces a Doppler shift in the spectrum (Vogt & Penrod 1983). Consequently, the stellar activity can induce large-amplitude RV variations that may have periodicities close to the stellar rotation period and therefore stellar activity can be misinterpreted as planetary signals. Several techniques have been developed over the past years to disentangle activity-induced variations and planetary signals. Some of these techniques are the study of correlations between activity indicators and RVs (see, e.g., Queloz et al. 2001; Boisse et al. 2011; Oshagh et al. 2017; Zechmeister et al. 2018), the selection of individual spectral lines less affected by activity (Dumusque 2018), and the use of Bayesian statistical models such as Gaussian processes (GP; Haywood et al. 2014; Rajpaul et al. 2015; Faria et al. 2016; Jones et al. 2017).

The spot- and facula-induced RV amplitude generally tends to decrease toward longer wavelengths (Desort et al. 2007). This is a consequence of the lower temperature contrast between heterogeneities and the quiet surface at longer wavelengths

★ Table A.1 and A.2 are only available at the CDS via anonymous ftp to `cdsarc.u-strasbg.fr` (`130.79.128.5`) or via `http://cdsarc.u-strasbg.fr/viz-bin/qcat?J/A+A/627/A116`

★★ S. Lalitha and D. Baroch contributed equally to this work.

(Barnes et al. 2011; Jeffers et al. 2014). However, in stars with strong magnetic fields the relative importance of the Zeeman effect increases with wavelength (Reiners et al. 2013). In addition, M dwarfs emit the bulk of their spectral energy at wavelengths redward of 1 μm (Reiners et al. 2010, and refernces therein). Hence, in theory, observations at wavelengths around 700–900 nm are ideal for both reducing the effect of stellar activity on RVs and minimizing the exposure time when surveying M dwarfs (Reiners et al. 2018b).

The high-resolution spectrograph CARMENES installed at the 3.5 m telescope at the Calar Alto Observatory (Almería, Spain) is specifically designed to cover a wide wavelength range (Quirrenbach et al. 2016, 2018). The CARMENES instrument extends further into the near-infrared (NIR) than most high-precision spectrographs to cover the range where M dwarfs emit the bulk of their spectral energy. The instrument consists of two cross-dispersed échelle spectrographs covering visible (VIS) wavelengths (0.52–0.96 μm, $R \sim 94\,600$) and NIR wavelengths (0.96–1.71 μm, $R \sim 80\,400$) (Quirrenbach et al. 2014). Since beginning its operation in January 2016, CARMENES has been regularly monitoring M dwarfs preselected from the CARMENES input catalog (Carmencita; Alonso-Floriano et al. 2015; Caballero et al. 2016; Reiners et al. 2018b). Several planetary systems around these objects have already been confirmed or discovered (Trifonov et al. 2018; Reiners et al. 2018a; Sarkis et al. 2018; Kaminski et al. 2018; Luque et al. 2018; Nagel et al. 2019; Perger et al. 2019), including a planetary companion orbiting Barnard's star (Ribas et al. 2018).

In this paper, we analyze the RV data of LSPM J2116+0234 and GJ 686, monitored as part of the CARMENES Guaranteed Time Observations (GTO) M dwarf survey. The data reveal the presence of a mini-Neptune around LSPM J2116+0234 with a period of 14.4 d. Furthermore, we used CARMENES data to refine the orbital parameters of GJ 686b reported by Affer et al. (2019; hereafter Aff19), a super-Earth with a period of 15.5 d. In Sect. 2, we introduce the basic properties of the host stars, and we describe the spectroscopic and photometric data in Sect. 3. In Sect. 4, we present our results from the analysis of RVs, photometry, and activity indicators. We model activity as correlated noise using a Bayesian framework to find the orbital parameters and discuss the stability of the signals through time and wavelength. We conclude and summarize our work in Sect. 5.

2. Targets

A summary of the basic stellar properties of both targets is presented in Table 1. The photospheric parameters such as the effective temperature $T_{\rm eff}$, surface gravity $\log g$, and metallicity [Fe/H] of the targets were determined in the CARMENES framework by Passegger et al. (2018) using the PHOENIX-ACES model grid (Husser et al. 2013). The stellar masses and radii were determined based on the photospheric parameters and a mass-radius relation.

LSPM J2116+0234 (Karmn J21164+025) is an M3.0 V star at a distance ~17.64 pc (Finch & Zacharias 2016; Gaia Collaboration 2016, 2018). It was discovered by Lépine & Shara (2005) as a northern star with a proper motion larger than 250 mas yr^{-1}, and was characterized photometrically and spectroscopically (Lépine & Gaidos 2011; Lépine et al. 2013; Gaidos et al. 2014). LSPM J2116+0234 has been identified as a nearby potential target for planet searches (Frith et al. 2013; Finch et al. 2014), activity analyses (Newton et al. 2017; Jeffers et al. 2018), and determination of photospheric stellar parameters (Passegger et al. 2018).

Table 1. Basic properties of the host stars.

Parameters	LSPM J2116+0234	GJ 686	Ref.
Karmn [a]	J21164+025	J17378+185	
α (J2000)	21:16:27.28	17:37:53.35	*Gaia*
δ (J2000)	+02:34:51.40	+18:35:30.16	*Gaia*
d (pc)	17.64 ± 0.02	$8.16 \pm 2{\cdot}10^{-3}$	*Gaia*
G (mag)	$10.8595 \pm 8{\cdot}10^{-4}$	$8.7390 \pm 6{\cdot}10^{-4}$	*Gaia*
J (mag)	8.219 ± 0.032	6.360 ± 0.023	2MASS
Sp. Type	M3.0 V	M1.0 V	PMSU
$T_{\rm eff}$ (K)	3475±51	3654 ± 51	Pas18
$\log g$ (cgs)	4.95 ± 0.07	4.88 ± 0.07	Pas18
[Fe/H] (dex)	-0.05 ± 0.16	-0.22 ± 0.16	Pas18
L ($L_\odot$)	$0.0247 \pm 3{\cdot}10^{-4}$	$0.0293 \pm 7{\cdot}10^{-4}$	Sch19
R ($R_\odot$)	0.431 ± 0.015	0.427 ± 0.017	Sch19
$M_\star$ ($M_\odot$)	0.430 ± 0.031	0.426 ± 0.033	Sch19
pEW (Hα) (Å)	$+0.004 \pm 0.005$	-0.128 ± 0.03	Jef18
$v \sin i$ (km s^{-1})	<2	<2	Rei18
$\log R'_{HK}$	...	-5.42 ± 0.05	Sua18
U (km s^{-1})	-23.99 ± 0.21	-33.56 ± 0.28	*Gaia*
V (km s^{-1})	-18.12 ± 0.29	35.40 ± 0.25	*Gaia*
W (km s^{-1})	-5.24 ± 0.21	-21.20 ± 0.17	*Gaia*

Notes. [a] CARMENES identifier.
References. 2MASS: Skrutskie et al. (2006); Cor16: Cortés-Contreras (2016); *Gaia*: Gaia Collaboration (2016, 2018); Jef18: Jeffers et al. (2018); Rei18: Reiners et al. (2018b); PMSU: Hawley et al. (1996); Pas18: Passegger et al. (2018); Sch19: Schweitzer et al. (2019); Sua18: Suárez Mascareño et al. (2018); UCAC4: Zacharias et al. (2013).

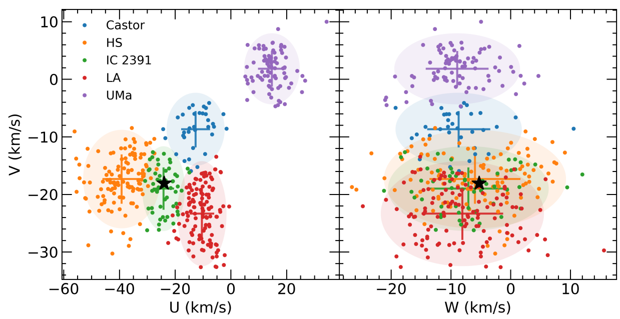

Fig. 1. (U,V) and (W,V) planesof young moving groups along with LSPM J2116+023 (star symbol). The crosses are the 1 sigma value for each moving group while the ellipses represents a 2 sigma value.

Cortés-Contreras (2016) computed Galactocentric space velocities consistent with membership to the young disk population and the IC 2391 stellar kinematic group. We evaluated the membership of LSPM J2116+0234 to the young disk population and the IC 2391 supercluster using the *Gaia* second data release (GDR2) astrometric data, and the RV as published by Reiners et al. (2018b). In Fig. 1, we compare the UVW velocities of LSPM J2116+0234 with known members of young moving groups from Montes et al. (2001). However, the lack of Hα feature in emission (pEW(Hα) = +0.004 ± 0.005 Å; Jeffers et al. 2018) seems to be inconsistent with the mean age of the supercluster. The Hα line can be seen in all members with similar spectral types of the IC 2391 open cluster. This cluster is thought to be the birthplace of the supercluster (Eggen 1995) and, hence, to have a similar age (50 ± 5 Myr; Barrado y Navascués et al. 2004). Besides, we do not detect any X-ray emission based on ROSAT All Sky Survey data. Therefore, we estimate the upper-limit luminosity $L_X < 10^{27}$ erg s^{-1}, which is lower than the expected value of $L_X < 10^{29}$ erg s^{-1} found for the members with similar spectral type of the IC 2391 and other older young open clusters such as the Pleiades or Hyades (Patten & Simon 1996). Furthermore, the tentative rotational period of about ∼42 d, obtained in this work (see Sect. 4.1), is longer than those of the IC 2391 cluster members (Patten & Simon 1996) and those of the members of the older Pleiades open cluster (110–120 Myr; Dahm 2015), which have typical rotational periods of less than ten days (Rebull et al. 2016). Therefore, although LSPM J2116+0234 shares the same kinematics as the IC 2391 supercluster, all the activity indicators and the rotation period indicate that the object is older than 50 Myr. In fact, from the gyrochronologic relation in Barnes (2007), we estimate an age for this star of ∼2 Gyr, using its rotation period and $B - V$ color.

GJ 686 (BD+18 3421, Karmn J17378+185) is an M1.0 V star located in the Hercules constellation at only d∼8.2 pc (Gaia Collaboration 2016, 2018). Because of its earlier spectral type and closer heliocentric distance, GJ 686 is also brighter than LSPM J2116+0234. In particular, its bright visual magnitude V ≈ 9.6 mag (Koen et al. 2010; Zacharias et al. 2013) enabled the star to be tabulated in the "Bonner Durchmusterung des südlichen Himmels" by Schönfeld (1886), and its parallax to be measured more than 100 yr ago (Barnard 1913; Adams et al. 1926; Osvalds 1957). It was one of the first late-type stars for which RV and metallicity were measured (Wilson 1953; Tokovinin 1990) and one of the first M-type standard stars (Henry et al. 1994). Later, GJ 686 took on greater relevance with the investigation of its moderate activity level (Stauffer & Hartmann 1986; Stephenson 1986; Herbst & Layden 1987; Rutten et al. 1989; Panagi & Mathioudakis 1993). Its moderate activity level has been confirmed by more recent, comprehensive studies (Delfosse et al. 1998; Wright et al. 2004; Isaacson & Fischer 2010; Jeffers et al. 2018) and is consistent with its kinematic classification as a thin-disk star (Cortés-Contreras 2016). In the past 20 yr several spectra were taken with HIRES on the Keck-I telescope to search for extrasolar planets around it. Using these data, Butler et al. (2017) found a signal at 15.5303 ± 0.0030 d and an amplitude of 3.46 ± 0.56 m s^{-1}, which they listed as a signal requiring confirmation. Recently, Aff19 analyzed high-precision RV data from HIRES together with HARPS and HARPS-N spanning over 20 yr, yielding the detection of a super-Earth orbiting GJ 686. The planetary companion was reported to have a minimum mass of $7.1 \pm 0.9\, M_\oplus$, orbiting its host star with a period of 15.5321 d and a semimajor axis of 0.091 au. Furthermore, they also analyzed the activity indicators of HIRES, HARPS, and HARPS-N, from which they estimated a rotation period of 37 d and an activity cycle of ∼2000 d.

3. Observations

3.1. Spectroscopic data

High-resolution spectroscopic observations were obtained with the VIS and NIR channels of the CARMENES spectrograph. The wavelength calibration of both channels is done with hollow-cathode lamps (U-Ar, U-Ne, Th-Ne) and temperature-pressure stabilized Fabry–Pérot etalons (Schäfer et al. 2018) to interpolate the wavelength solution and monitor any instrumental drift during observations (Bauer et al. 2015). Reduction of raw spectra is automatically performed using the CARACAL (CARMENES Reduction and Calibration; Caballero et al. 2016) pipeline, which corrects for bias, flat-field, and cosmic rays.

High-precision RVs are routinely computed by the CARMENES SERVAL pipeline (Zechmeister et al. 2018), using an algorithm based on a least-squares fitting of the RV shifts of the individual spectra against a high signal-to-noise ratio (S/N) template, which is constructed by co-adding all available spectra of the target (see also Anglada-Escudé & Butler 2012). A nightly zero-point correction is applied to the RVs to track remaining systematics of the instrument and/or pipeline (for more details see Trifonov et al. 2018; Tal-Or et al. 2019). These nightly zero-points are calculated using all the CARMENES GTO stars with an RV standard deviation lower than 10 m s^{-1}. The median magnitude of these corrections are 1.79 and 1.78 m s^{-1} for the VIS and NIR channel data of LSPM J2116+0234, respectively, and 1.86 m s^{-1} for the VIS channel data of GJ 686.

Telluric contamination and unmasked detector defects can lead to systematic RV errors in spectral orders with low RV content. Therefore, we carefully selected the orders to exclude from our computation of the NIR RVs. We carried out this process iteratively to minimize the sample rms of the entire CARMENES M-dwarf sample.

The SERVAL pipeline also provides information about stellar activity such as line indices for a number of spectral features (e.g., Hα, Na I D, and Ca II IRT), the differential line width (dLW), and the chromatic index (CRX), as defined in Zechmeister et al. (2018). Furthermore, for each CARMENES spectrum, the cross-correlation function (CCF) is computed using a weighted mask of co-added stellar spectra. The CCFs are fitted with a Gaussian function to determine the contrast, the full width at half maximum (FWHM), and the bisector velocity span (BIS). A detailed description on CCF computation methodology is given by Reiners et al. (2018a).

LSPM J2116+0234 was monitored between 30 June 2016 and 29 November 2018, obtaining 72 and 57 high-resolution spectra from the CARMENES VIS and NIR channels, respectively. In total, the observations cover a time span of 882 d, with typical exposure times of 1800 s. In Table 2, we provide a summary of the total number of available RVs, the time span of the data, standard deviation, and median internal uncertainty $\overline{\sigma}$.

For GJ 686, 100 CARMENES spectra from the VIS channel are available, which were obtained between 22 February 2016 and 29 November 2018, covering 987 d. Besides, as outlined in Aff19, other instruments have monitored GJ 686 during the past 21 yr, adding an additional 198 precise RVs.

To avoid using RV epochs contaminated by flares or spectra with a low S/N, we applied a 3σ clipping to both the RVs and errors of each individual dataset, removing a total of 10 RVs from GJ 686 (3.5%) and 4 from LSPM J2116+0234 (3.1%). Since the internal RV precision in the NIR is larger than the expected RV signal for GJ 686, we decided not to use the NIR RVs. In Fig. 2, we show the RV time series of both targets. The radial velocities for LSPM J2116+0234 and GJ 686 are given in Table A.1 and A.2, respectively.

3.2. Photometric data

Several potential exoplanet candidates from CARMENES are monitored photometrically by ground-based telescopes to constrain the stellar rotation (Díez Alonso et al. 2019) and to search for planetary transits. LSPM J2116+0234 was not monitored by our photometric follow-up program, therefore, we searched through the archival surveys such as All-Sky Automated Survey (ASAS[1]; Pojmański 1997) and Catalina Sky Survey[2]

[1] http://www.astrouw.edu.pl/asas/
[2] https://catalina.lpl.arizona.edu

Table 2. Basic information of archival and CARMENES observations.

Target	Instrument	N_{obs} (N_{used}) (#)	Δt (d)	rms (m s^{-1})	$\overline{\sigma}$ (m s^{-1})
LSPM J2116+0234	CARM-VIS	72(70)	882	5.30	1.48
	CARM-NIR	57(55)	823	6.89	6.54
GJ 686	HIRES	114(112)	5947	4.09	1.85
	CARM-VIS	100(96)	987	3.11	1.71
	HARPS-N	64(61)	1347	3.02	0.71
	HARPS	20(19)	2299	2.42	0.69

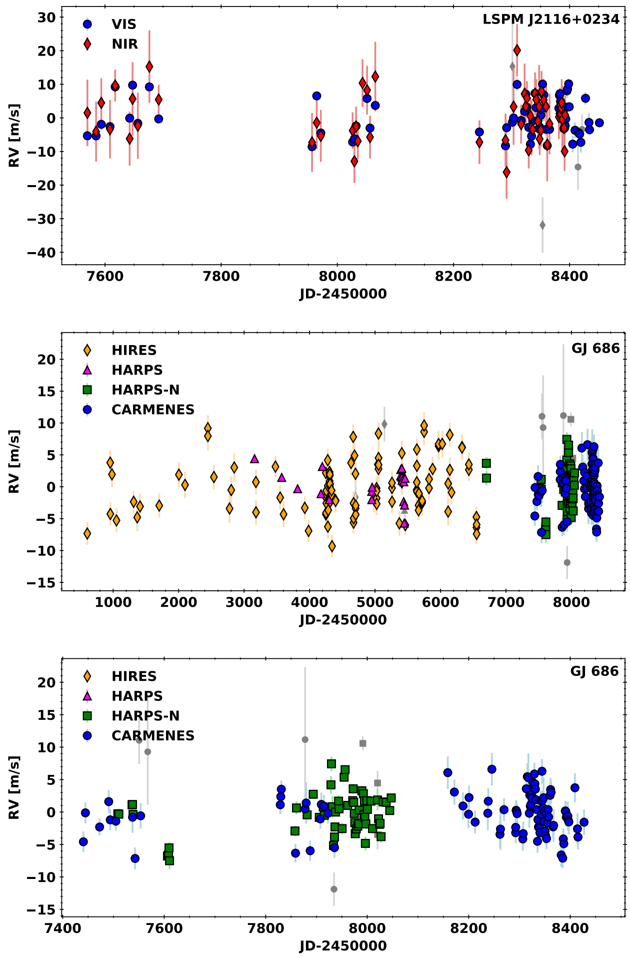

Fig. 2. Radial velocity time series of the M-dwarf stars LSPM J2116+0234 (*top*), GJ 686 (*middle*), and zoom on the data with JD>2457000 of GJ 686 (*bottom*). The gray symbols correspond to the clipped RVs.

(Drake et al. 2009). These survey data were used to investigate the stellar rotation period.

Along with the photometry from the ASAS database, we monitored GJ 686 with the following facilities:

- MONET: the MONET 1.2 m telescope located at the Sutherland station of the South African Astronomical Observatory (SAAO). It is equipped with a 2k × 2k CCD with a plate scale of 0.36 arcsec per pixel.
- SNO: the T90 telescope located at Sierra Nevada Observatory, Spain is a 0.9 m Ritchey-Chrétien telescope. It is equipped with a CCD camera VersArray 2k × 2k with a plate scale of 0.38 arcsec per pixel (Rodríguez et al. 2010).
- TJO: the Joan Oró telescope is located at the Montsec Astronomical Observatory (OAdM), Spain. It is a fully robotic 0.8 m Ritchey-Chrétien telescope with an FLI PL4240 2k × 2k camera and a plate scale of 0.36 arcsec per pixel.
- LCOGT: the Las Cumbres Observatory Global Telescope is a network of robotic telescopes deployed at several sites around the globe. The observations were performed using the 0.4 m telescopes in Haleakala, Hawai'i (kb27 and kb82 SBIG CCDs), the Teide Observatory in Tenerife (kb23 and kb99 SBIG CCDs), the McDonald Observatory in Texas (kb92 SBIG CCDs), the South African Astronomical Observatory (kb96 SBIG CCDs), and the Cerro Tololo Interamerican Observatory (kb 81 SBIG CCDs). The telescopes have a plate scale of 0.57 arcsec per pixel.

In Table 3, we give the detailed photometric observation log for GJ 686. The MONET, TJO, and SNO photometric data were reduced and analyzed with standard packages and tasks of the Image Reduction and Analysis Facility (IRAF)[3]. The LCOGT images were reduced by the BANZAI pipeline (McCully et al. 2018). The differential photometry was performed by dividing the flux of GJ 686 by the combined flux of all comparison stars.

4. Analysis and results

4.1. LSPM J2116+0234

To investigate the RV variability of LSPM J2116+0234, we computed the generalized Lomb-Scargle (GLS) periodogram (Zechmeister & Kürster 2009) of the RVs from the individual VIS and NIR CARMENES channels and from the combined dataset. In Fig. 3a, the resultant periodograms are plotted together with the window function (WF) of the combined dataset (top panel). We computed the false alarm probability (hereafter, FAP) levels of 10, 1, and 0.1% using 10 000 bootstrap randomizations of the input data. The signal is considered significant if it reaches a FAP level <0.1%. The VIS data periodogram (Fig. 3a, second panel) displays a significant and isolated signal at 0.0692 d^{-1} (14.445 d), accompanied by the two yearly aliases at ±0.0027 d^{-1} (~365 d) from the central peak, as suggested by the WF. The NIR data, shown in the third panel of Fig. 3a also indicate a signal at 14.44 d just above the 1% FAP level. Because of the larger errors of the NIR RVs, the periodogram of the combined dataset (Fig. 3a, bottom panel) is very similar to the periodogram of the VIS channel. The combined periodogram also has a very significant peak at 14.436 d. Furthermore, we also find another significant signal at a period of 0.9308 d^{-1} (1.07 d), which is the expected period of a daily alias of the 14.436 d signal.

We analyzed the periodograms of the residuals after subtracting the main signal from the RV periodograms to investigate if there are significant RV variations remaining. The residual periodograms are shown in Fig. 3b. They show a significant peak in the VIS data at 0.0230 d^{-1} (41.8 d), and 0.0232 d^{-1} (43.1 d) at the 1% FAP level in the combined dataset. However, the NIR data do not show any signal above the 10% FAP level.

Furthermore, we carried out a periodogram analysis of the activity indicators to investigate if the signals at ~14.44 and

[3] IRAF is distributed by the National Optical Astronomy Observatory, which is operated by the Association of Universities for Research in Astronomy under a cooperative agreement with the National Science Foundation. http://iraf.noao.edu/

Table 3. Photometric observation log of GJ 686.

	Monet-S Sutherland	SNO Granada	TJO Lleida	LCO Global network
Latitude	−32°22′44″	+37°03′51″	+42°03′05″	
Longitude	+20°48′39″	−03°23′05″	+00°43′46″	
Altitude (m)	1700	2896	1568	
Filters (Johnson)	*B*	*V*, *R*	*R*	*B*, *V*
FOV (arcmin)	12.6 × 12.6	13.2 × 13.2	12 × 12	19 × 29
Exposure time (s)	2 (*B*)	25 (*V*), 10 (*R*)	20 (*R*)	72 (*B*), 17 (*V*)
Number of nights (d)	26	26	38	69
Time Span (d)	65	58	87	93
Observation period (2018)	July–September	July–September	July–October	July–October

Notes. For LCO node positions see https://lco.global/observatory/sites/. Epochs with long duration observation with LCO was exposed to 5s in *V* filter.

∼42 d in the RV data may have a stellar origin. We show the resulting GLS periodograms of the activity indicators and the properties of the CCFs in Fig. 4. None of the periodograms show any significant peak at 14.436 d (vertical solid line). The calcium triplet lines show significant peaks between 41 and 44 d (vertical dashed line). These peaks are close to the significant peak in the residual RV periodogram. At 1% FAP level, the Hα index shows a peak at 41.8 d, and the CRX at 48.0 d, which has a higher power than its yearly alias at 42.4 d. We interpret this yearly alias as the real signal due to its consistency with the signals found on the other indicators. On subtraction of these signals, the residuals do not show any significant peaks in their periodograms (see Fig. A.2). Thus, we attribute the signals at ∼42 d in the RV residuals and the activity indices to be related to the rotation period of the star.

We investigated whether there is any significant correlation between the RVs and various activity indicators (Fig. A.6). None of the indicators show a correlation above the significance limit, which we set as a *p*-value of 0.05 or lower, except for one of the Ca II IRT lines with a *p*-value of 0.025. Further, we can see a color gradient in the correlation plot of this line, indicating that the correlation is indeed caused by the rotation period. We also observe that there are indicators, which despite having significant signals in the periodogram, show no correlation with the RV, which could be indicative of shift in phase between indicator and RV (0 or π).

The analysis of the CARMENES RVs was complemented with the archival photometric data for LSPM J2116+0234. Figure 5a shows the observations from ASAS spanning ∼9 yr and Catalina spanning ∼8.5 yr with an overlap of ∼4.5 yr. The GLS periodograms of the photometric data are depicted with bootstraped FAP levels (Fig. 5b). We do not find prominent signals around the planetary period or the activity indicator peaks found in the RV data. However, the Catalina dataset shows a significant period near 45 d. After removing this signal, no prominent period can be found in the data. In contrast, we find a significant signal close to the 14 d signal in the ASAS data at ∼13.03 d. However, the ASAS WF shows a significant period of about 13.80 d. After removing the signal at 13.80 d, the signal at 13.03 d also disappears. Furthermore, the remaining signals do not reach the 10% FAP level, with a second signal at ∼45 d.

We note that between HJD∼2 453 400 and 2 455 100 d there are overlapping observations by ASAS and Catalina. We analyzed these datasets during the overlapping period together applying an offset to both the datasets. However, we do not find any significant period.

To summarize, based on CARMENES VIS and NIR RV data we identify a strong signal at ∼14.44 d with no counterpart in the activity indicators, which we attribute to a planetary origin. We also find significant signals at ∼42 d in the residuals of the RV data. This signal is also significant in some activity indicators, and thus we relate it to the rotation period of the star.

4.1.1. Keplerian modeling

Assuming that the strong signal at 14 d has planetary origin, we determined the orbital parameters of the signal by fitting a Keplerian model with semi-amplitude (K), eccentricity (e)[4], orbital period (P), longitude of periastron (ω), time of periastron passage[5] (T_0), and an RV offset for each channel ($\gamma_{\rm INS}$) as free parameters. Furthermore, we also allowed an adjustable RV jitter for each set of RVs ($\sigma_{\rm jit;INS}$) in the fit, as defined by Baluev (2009).

We computed the uncertainties and final orbital parameters by running the Markov chain Monte Carlo (MCMC) sampler `emcee` (Foreman-Mackey et al. 2013), with the natural logarithm of the model likelihood as the objective function. We run 500 chains of 15 000 steps each, with a burn-in of 10 000. The uncertainties were derived from the 1σ (68.3%) confidence interval of the posterior parameter distribution. We chose uniform priors as those shown in the last columns in Tables 4 and 5.

The best model parameters for the VIS, NIR, and the combined dataset can be found in Table 4. To test the consistency of the signals in both datasets, we modeled a Keplerian orbit for each one separately. The Keplerian model parameters of the NIR channel, listed in the fifth column in Table 4, resulted in an $e \sin\omega$ and $e \cos\omega$ compatible with zero, so we fixed their values to those obtained with the VIS channel, which is shown in the third column of Table 4. All the orbital parameters are compatible within their respective uncertainties. The jitter in the VIS channel is slightly higher than in the NIR channel, indicating that the unaccounted errors are larger (e.g., from stellar variability).

The best-fit parameters of the combined dataset correspond to a planet with a minimum mass of $13.3^{+1.0}_{-1.1}\,M_\oplus$ orbiting its host star every $14.4399^{+0.0078}_{-0.0087}$ d with an eccentricity of $0.183^{+0.062}_{-0.063}$ causing a RV semi-amplitude of $6.26^{+0.41}_{-0.39}$ m s^{-1}.

[4] $e^2 = (e \sin\omega)^2 + (e \cos\omega)^2$.

[5] For a circular orbit, we define it as the time of maximum RV.

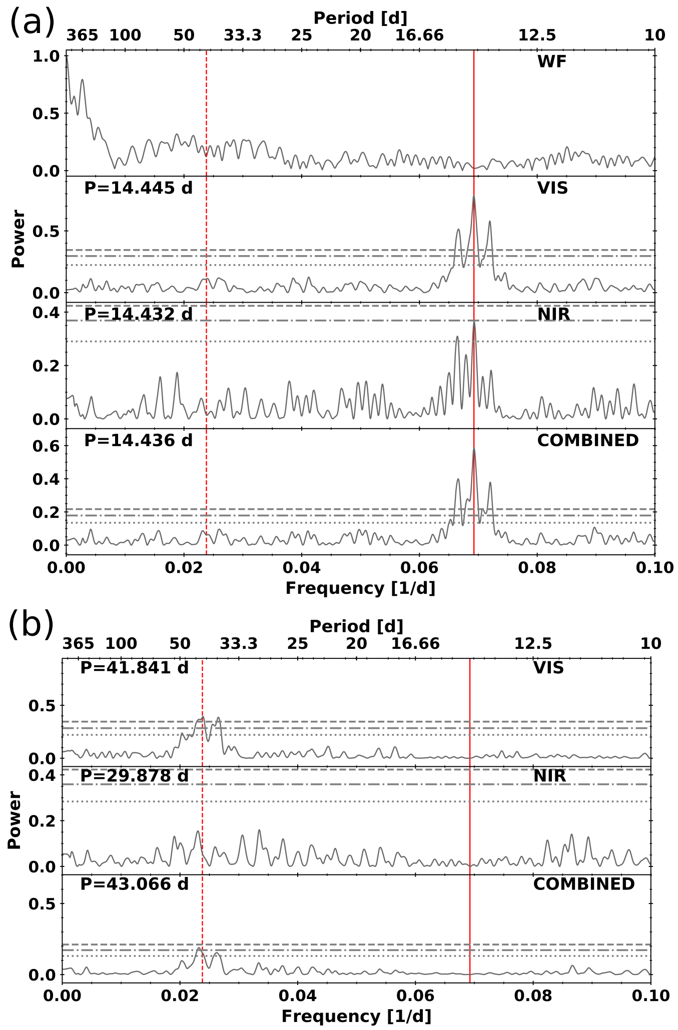

Fig. 3. (*a*) Generalized Lomb-Scargle periodograms of LSPM J2116+0234 RV data. The *top panel* shows the WF of the combined dataset. The *next two panels* correspond to the VIS and the NIR CARMENES channels, respectively, while the *bottom panel* shows the periodogram of the combined dataset. The horizontal lines represent bootstrapped FAP levels of 10, 1, and 0.1%. The periods reported in each panel refer to the highest peak. The vertical solid and dashed red lines indicate the period of the proposed planet and the estimated stellar rotation period at 14.44 and ∼42 d, respectively. Although we inspected the periodogram for significant signals at frequencies up to 1 d^{-1}, for visual purposes, we only show the region from 0 to 0.1 d^{-1} in all the periodograms. (*b*) GLS periodograms of the RV residuals after removing a sinusoid with the period found in (a).

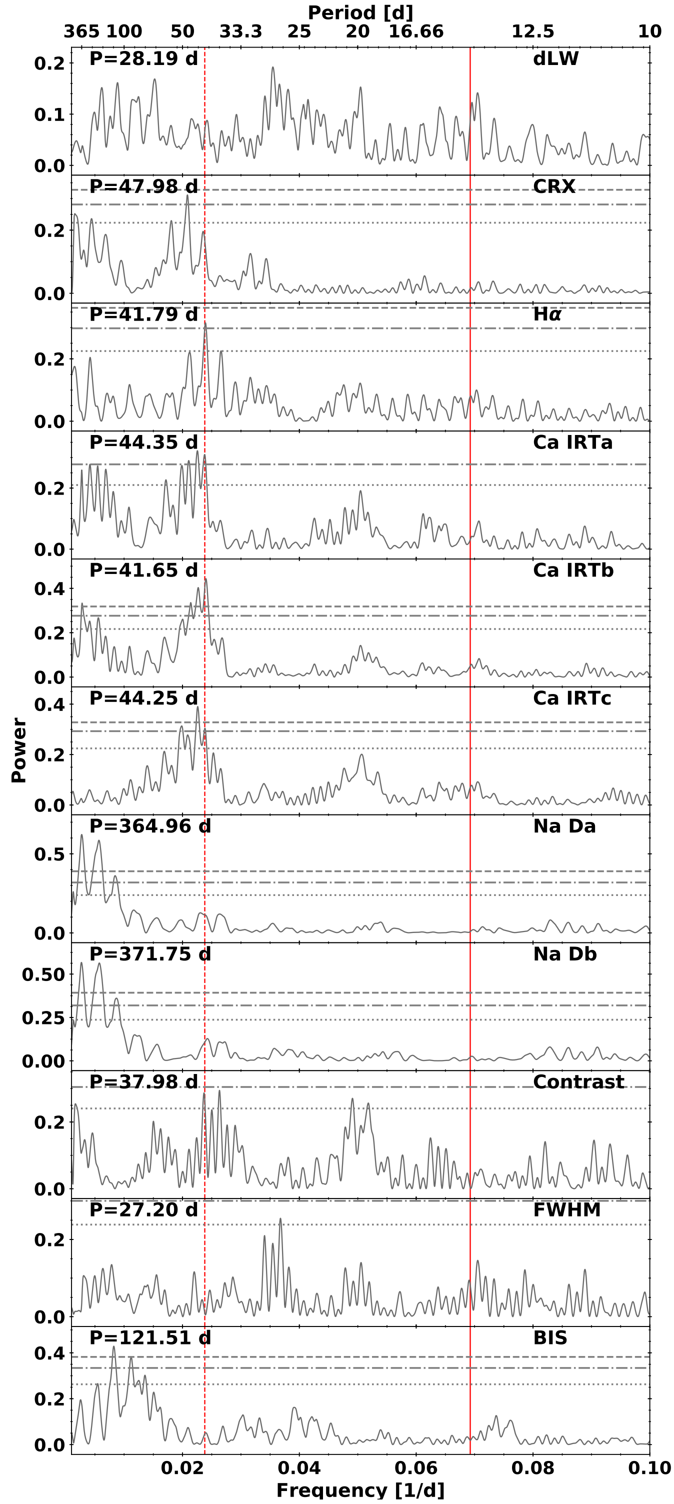

Fig. 4. Generalized Lomb-Scargle periodograms of the activity indicators of LSPM J2116+0234. The vertical red solid line indicates the period of the suggested planet, while the vertical red dotted indicates the stellar rotation period. The periods reported in each panel refer to the highest peak. Horizontal lines represent the bootstrapped 10, 1, and 0.1% FAP levels.

4.1.2. Model comparison and signal stability

To evaluate the statistical significance of our model, we computed the improvement in the natural logarithm of the likelihood ($\Delta \ln L$). The likelihood function is the probability distribution of the data fitting the model and depends on the adopted noise model (see, e.g., Baluev 2013; Ribas et al. 2018).

We consider two different noise models: a white-noise model, which assumes that all the measurements are statistically independent from each other (null model); and a correlated-noise model using a GP, which parametrizes the covariance function correlating all the measurements. Rasmussen & Williams (2005) described many different covariance functions with different properties, among which the quasi-periodic harmonic oscillator has been widely used to disentangle planetary signals from stellar activity signals (Haywood et al. 2014; Mortier et al. 2018; Perger et al. 2019) or even to infer stellar rotation periods (Angus et al. 2018).

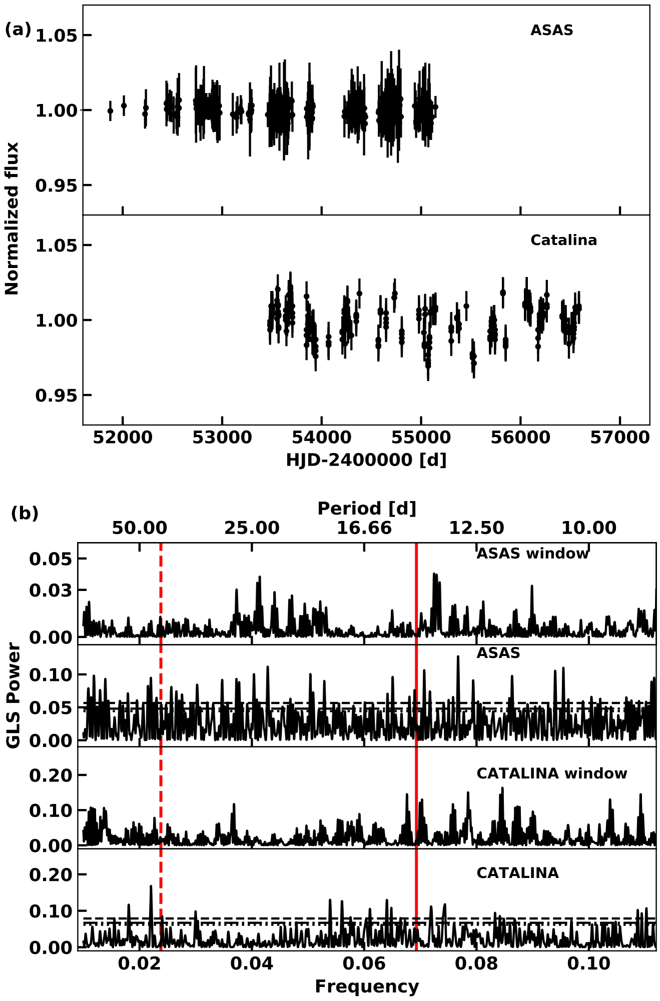

Fig. 5. (*a*) Photometric time series of LSPM J2116+0234 observed with ASAS and Catalina surveys. (*b*) Generalized Lomb-Scargle periodograms of the photometric time series of LSPM J2116+0234 observed with ASAS and Catalina surveys. The WFs for each of the surveys are plotted. The vertical solid and dashed lines indicate the planetary period and estimated stellar rotation period at 14.44 and ~42 d, respectively. The horizontal lines represent 10, 1, and 0.1% bootstrapped FAP levels, respectively.

For the null model, we assume that the data variation is produced by uncorrelated noise, and thus we only fit the offset and a jitter term for each different dataset. We computed the final parameters and uncertainties running the MCMC sampler `emcee`. The null model solution is shown in the second column of Table 4, which gives jitter terms with higher values than for the other models, especially in the VIS, pointing toward an extra RV variability that is unaccounted by the measurement uncertainty. We obtain a best-fit $\ln L = -400.0$, which we take as the base value to compute the $\Delta \ln L$ of the other models in Table 4.

We investigated the influence of the activity-induced RV variations on the determination of the orbital parameters by modeling together a Keplerian orbit and an activity term with a GP, which uses the quasi-periodic function as the covariance matrix. This function is characterized by four hyperparameters: (1) the output-scale amplitude $K_{\rm QP}$, which contains the amplitude of the RV variations due to the activity; (2) the decay time $\lambda_{\rm QP}$, which is related to the lifetime of the active regions; (3) the smoothing parameter $w_{\rm QP}$, which controls the high-frequency noise, and may be related to the number of spots or facule in the photosphere; and (4) the periodicity of the correlations $P_{\rm QP}$, which is usually interpreted as the rotation of the star. We modeled the data of each instrument with separate GPs sharing all the parameters except the amplitude $K_{\rm QP}$, which should be different for instruments working in various wavelength ranges. This model is implemented using the `george` python library (Ambikasaran et al. 2015). We modeled the Keplerian orbit with the same parameters as those used in Sect. 4.1.1, including also a different RV offset and a jitter term for each instrument. All the parameters were optimized simultaneously, and their solutions and uncertainties were computed from the MCMC posterior distribution. We consider a model as tentative or as statistically significant over the null model if it reaches a FAP level of 1% or 0.1%, respectively. These values corresponds to $\Delta \ln L = 15.1$ and 18.7, which are computed from a bootstrap randomization of 5000 permutations of the datapoints.

The parameters of the solution for the activity plus Keplerian modeling of the combined dataset of LSPM J2116+0234 are shown in the seventh column of Table 4. The orbital parameters are very similar to the values obtained with only a Keplerian model. We note that all the parameters agree within 1σ uncertainties, except for the jitter term in the VIS channel, which is smaller. This is expected since we are adding an extra term modeling the activity, which was included as part of the jitter term previously. As for the GP hyperparameters, we find a periodicity of $P_{\rm GP} = 42.0^{+2.0}_{-1.5}$ d, which is very similar to the periodicities found in the activity indicators. Hence, we consider the period of ~42 d as the rotation period of the star. The amplitude of the activity RV term variations is $1.86^{+0.49}_{-0.40}$ m s^{-1} in the VIS channel, while it is nearly zero in the NIR. This is in agreement with the expected decrease of the activity signal toward longer wavelengths, but could also be produced by the larger uncertainties of this channel. We note that the GP model with activity term is favored over the null model and over the Keplerian model and there is an increase of the logarithm of the likelihood of 80.4 and 16.5, respectively.

We investigated whether the NIR RVs are modifying significantly the VIS RV solution. We fit a Keplerian plus an activity term to the VIS RVs alone, whose best parameters are shown in the fourth column in Table 4. All the parameters are compatible within one sigma. Thus, although the NIR RVs have internal uncertainties higher than the planet signal does not affect significantly the orbital solution given by the VIS RVs.

As a consistency check between GP models, we also used `celerite`, the fast and scalable GP regression package (Foreman-Mackey et al. 2017), which uses as covariance matrix the model of a stochastically driven simple harmonic oscillator (Kaminski et al. 2018; Ribas et al. 2018). This model is characterized by the damping time τ, the oscillator frequency P_0, and the height of the peak S_0. The parameter S_0 scales with the power of the associated frequency. The eighth column in Table 4 shows the best-fit parameters using this model, which gives compatible periods for the planet and rotation of the star.

In Fig. 6, we show the phased RV data with the best-fit Keplerian model (top panel) and Keplerian+GP (bottom panel). The posterior distribution of the parameters and their correlations of the best-model solution are depicted in Fig. A.4. The histograms suggest that all the orbital parameters follow a well-behaved normal distribution, except for the expected correlation between T_0 and $e \sin \omega$ and $e \cos \omega$ because of their proximity to the degenerate solution at zero eccentricity.

Finally, we checked the stability of the signals throughout the wavelength range covered to provide more evidence against

Table 4. Best-fit parameters to different models of the planetary system LSPM J2116+0234b.

	LSPM J2116+0234 b							
	VIS+NIR	VIS		NIR	VIS+NIR			Prior
	Null model	Keplerian	GP + Keplerian `George`	Keplerian	Keplerian	GP + Keplerian `George`	GP + Keplerian `Celerite`	
Planetary parameters								
P (d)	...	$14.4432^{+0.0080}_{-0.0086}$	$14.4433^{+0.0079}_{-0.0086}$	$14.425^{+0.030}_{-0.029}$	$14.4399^{+0.0078}_{-0.0087}$	$14.4410^{+0.0076}_{-0.0088}$	$14.451^{+0.012}_{-0.010}$	$\mathcal{U}(10, 20)$
T_0 [JD-2457000]	...	$573.36^{+1.05}_{-0.99}$	$573.27^{+0.94}_{-0.87}$	$574.7^{+1.3}_{-1.3}$	$573.6^{+1.1}_{-1.1}$	$573.34^{+0.87}_{-0.90}$	$572.52^{+0.75}_{-0.88}$	$\mathcal{U}(550, 590)$
K (m s^{-1})	...	$6.43^{+0.45}_{-0.42}$	$6.31^{+0.44}_{-0.43}$	$5.1^{+1.3}_{-1.3}$	$6.26^{+0.41}_{-0.39}$	$6.19^{+0.38}_{-0.40}$	$6.29^{+0.25}_{-0.29}$	$\mathcal{U}(0, 20)$
$e \sin \omega$	...	$-0.069^{+0.068}_{-0.070}$	$-0.081^{+0.059}_{-0.053}$	−0.069 (fixed)	$-0.066^{+0.066}_{-0.067}$	$-0.084^{+0.054}_{-0.050}$	$0.015^{+0.013}_{-0.014}$	$\mathcal{U}(-1, 1)$
$e \cos \omega$	...	$0.168^{+0.067}_{-0.066}$	$0.170^{+0.064}_{-0.065}$	0.168 (fixed)	$0.157^{+0.065}_{-0.065}$	$0.164^{+0.062}_{-0.060}$	$0.159^{+0.061}_{-0.064}$	$\mathcal{U}(-1, 1)$
a (AU)	...	$0.0876^{+0.0022}_{-0.0021}$	$0.0876^{+0.0021}_{-0.0021}$	$0.0876^{+0.0022}_{-0.0021}$	$0.0876^{+0.0022}_{-0.0021}$	$0.0876^{+0.0021}_{-0.0020}$	$0.0876^{+0.0020}_{-0.0021}$	...
$m_p \sin i$ ($M_\oplus$)	...	$13.6^{+1.1}_{-1.1}$	$13.4^{+1.1}_{-1.1}$	$10.8^{+2.9}_{-2.8}$	$13.3^{+1.0}_{-1.1}$	$13.1^{+1.0}_{-1.0}$	$13.56^{+0.54}_{-0.62}$	...
RV offsets and jitter								
$\gamma_{\rm VIS}$ (m s^{-1})	$0.27^{+0.64}_{-0.60}$	$0.41^{+0.30}_{-0.30}$	$0.00^{+0.55}_{-0.63}$	...	$0.41^{+0.30}_{-0.29}$	$-0.09^{+0.56}_{-0.62}$	$0.22^{+0.30}_{-0.26}$	$\mathcal{U}(-100, 100)$
$\gamma_{\rm NIR}$ (m s^{-1})	$0.12^{+0.91}_{-0.88}$	...	...	$-0.02^{+0.92}_{-0.89}$	$-0.02^{+0.90}_{-0.90}$	$0.03^{+0.93}_{-0.92}$	$0.15^{+0.35}_{-0.42}$	$\mathcal{U}(-100, 100)$
$\sigma_{\rm jit,VIS}$ (m s^{-1})	$5.1^{+0.53}_{-0.43}$	$1.83^{+0.31}_{-0.28}$	$0.42^{+0.59}_{-0.29}$	...	$1.87^{+0.31}_{-0.28}$	$0.35^{+0.36}_{-0.25}$	$0.67^{+0.31}_{-0.28}$	$\mathcal{U}(0, 10)$
$\sigma_{\rm jit,NIR}$ (m s^{-1})	$1.8^{+1.5}_{-1.2}$	...	...	$1.08^{+1.17}_{-0.77}$	$1.28^{+1.36}_{-0.88}$	$1.06^{+1.19}_{-0.74}$	$0.96^{+0.51}_{-0.28}$	$\mathcal{U}(-10, 10)$
Hyper-parameters								
$K_{\rm QP,VIS}$ (m s^{-1})	...	...	$1.80^{+0.48}_{-0.53}$	...	...	$1.86^{+0.49}_{-0.40}$	...	$\mathcal{U}(0.001, 10)$
$K_{\rm QP,NIR}$ (m s^{-1})	...	...	...	...	...	$0.04^{+0.54}_{-0.04}$	...	$\mathcal{U}(0.001, 10)$
$\lambda_{\rm QP}$ (d)	...	...	125^{+140}_{-72}	...	...	102^{+111}_{-55}	...	$\mathcal{U}(5, 500)$
$w_{\rm QP}$	...	...	$0.28^{+0.18}_{-0.16}$	...	...	$0.30^{+0.19}_{-0.11}$	...	$\mathcal{U}(0, 1)$
$P_{\rm QP}$ (d)	...	...	$42.1^{+2.5}_{-2.0}$	...	...	$42.0^{+2.0}_{-1.5}$	...	$\mathcal{U}(28, 56)$
P_0 (d)	...	...	...	...	...	...	$44.5^{+4.6}_{-7.0}$	$\mathcal{U}(1, 1500)$
τ (d)	...	...	...	...	...	...	480^{+390}_{-412}	$\mathcal{U}(1, 1500)$
S_0	...	...	...	...	...	...	$0.46^{+1.59}_{-0.39}$	$\mathcal{U}(-15, 15)$
Fit quality								
$\sigma_{\rm O-C}$ (m s^{-1})	4.64	2.44	1.31	5.49	4.14	3.85	3.93	...
$\ln L$	−400.0	−160.4	−144.36	−174.4	−336.1	−319.6	−322.3	...
$\Delta \ln L$	0	...	...	...	63.9	80.4	77.7	...

a potential activity-induced origin of the signals. The RVs from each spectral order of CARMENES were used to compute the orbital parameters of a circular orbit and their uncertainties from the final posterior distribution of an MCMC sample of 500 walkers and 1000 steps. In Fig. 7, we show the resulting semi-amplitude of the circular orbit as a function of the logarithm of the wavelength at the center of each CARMENES order. All the values are consistent within 2σ of the semi-amplitude found with the RVs of all the orders combined. Further, we do not see a decrease in amplitude toward longer wavelength, as would be expected if the signal is activity-induced. Therefore, we conclude that the signal at the ∼14.44 d period in LSPM J2116+0234 is consistent with the planet hypothesis.

4.2. GJ 686

To investigate the RV variability of GJ 686, we computed the GLS periodograms of the HIRES, HARPS, HARPS-N, and CARMENES measurements. In Fig. 8a (top to bottom), we show the WF of the combined dataset, the periodograms of the HIRES, HARPS, HARPS-N, and CARMENES RVs, and of all data combined. We subtracted the mean value of each RV dataset to compute the periodogram of the combined dataset. The horizontal lines indicate the 10, 1, and 0.1% bootstrapped FAP levels.

Except for HARPS, all the instruments have the strongest signal at a period of 15.5 d with FAP < 0.1%. The HARPS dataset shows a signal around 16.0 d just below the 10% FAP, although we also notice an excess power at ∼15.5 d. The periodogram of the combined dataset has a highly significant signal at 0.06439 d^{-1} (15.53 d). We notice an additional peak at 0.06165 d^{-1} (16.22 d) with high significance, owing to one yearly alias of the main signal, which is clearly observed in the WF.

We notice additional peaks with 1% FAP level at ∼49 d in the HIRES data and at ∼41 d in the CARMENES and combined datasets. This signal becomes significant in the combined dataset

Table 5. Best-fit parameters to various models of the planetary system Gl 686 b.

	Gl 686 b						
	Aff19	This work					
	`George`	Null model	Keplerian	Circular	GP + Keplerian `George`	GP + Keplerian `Celerite`	Prior
Planetary parameters							
P (d)	$15.5321^{+0.0017}_{-0.0017}$	...	$15.5311^{+0.0015}_{-0.0017}$	$15.5311^{+0.0015}_{-0.0015}$	$15.5314^{+0.0015}_{-0.0014}$	$15.5309^{+0.0017}_{-0.0015}$	$\mathcal{U}(10, 20)$
T_0 [JD-2450000]	$7805.69^{+0.28}_{-0.28}$	...	$605.8^{+9.5}_{-11.5}$	$610.83^{+0.63}_{-0.61}$	$606.8^{+1.8}_{-2.3}$	$605.2^{+4.1}_{-3.1}$	$\mathcal{U}(585, 625)$
K (m s^{-1})	$3.29^{+0.31}_{-0.32}$	...	$2.85^{+0.21}_{-0.22}$	$2.83^{+0.22}_{-0.22}$	$3.02^{+0.18}_{-0.20}$	$3.11^{+0.28}_{-0.29}$	$\mathcal{U}(0, 20)$
$e \sin \omega$	...	...	$-0.019^{+0.092}_{-0.098}$	...	$-0.077^{+0.056}_{-0.058}$	$0.009^{+0.007}_{-0.006}$	$\mathcal{U}(-1, 1)$
$e \cos \omega$	...	...	$-0.012^{+0.070}_{-0.082}$	...	$0.001^{+0.056}_{-0.064}$	$0.079^{+0.060}_{-0.051}$	$\mathcal{U}(-1, 1)$
a (AU)	0.091 ± 0.004	...	$0.0917^{+0.0024}_{-0.0023}$	$0.0917^{+0.0024}_{-0.0023}$	$0.0917^{+0.0024}_{-0.0023}$	$0.0917^{+0.0023}_{-0.0023}$	...
$m_{\rm p} \sin i$ ($M_\oplus$)	7.1 ± 0.9	...	$6.22^{+0.60}_{-0.61}$	$6.24^{+0.58}_{-0.59}$	$6.64^{+0.53}_{-0.54}$	$6.89^{+0.89}_{-0.87}$	...
RV offsets and jitter							
$\gamma_{\rm HIRES}$ (m s^{-1})	$0.65^{+0.52}_{-0.49}$	$-0.12^{+0.35}_{-0.37}$	$-0.05^{+0.32}_{-0.32}$	$-0.08^{+0.32}_{-0.33}$	$0.07^{+0.56}_{-0.57}$	$0.05^{+0.45}_{-0.47}$	$\mathcal{U}(-100, 100)$
$\gamma_{\rm HARPS}$ (m s^{-1})	$-0.33^{+0.60}_{-0.61}$	$0.15^{+0.56}_{-0.53}$	$0.11^{+0.46}_{-0.46}$	$0.12^{+0.40}_{-0.43}$	$0.59^{+0.63}_{-0.66}$	$0.12^{+0.72}_{-0.80}$	$\mathcal{U}(-100, 100)$
$\gamma_{\rm HARPS-N}$ (m s^{-1})	$-0.41^{+0.53}_{-0.63}$	$-0.19^{+0.38}_{-0.39}$	$-0.11^{+0.29}_{-0.28}$	$-0.10^{+0.29}_{-0.28}$	$-0.41^{+0.68}_{-0.64}$	$-0.33^{+0.41}_{-0.47}$	$\mathcal{U}(-100, 100)$
$\gamma_{\rm CARM}$ (m s^{-1})	...	$-0.34^{+0.32}_{-0.31}$	$-0.44^{+0.28}_{-0.28}$	$-0.43^{+0.26}_{-0.26}$	$-1.11^{+0.63}_{-0.65}$	$-1.09^{+0.66}_{-0.67}$	$\mathcal{U}(-100, 100)$
$\sigma_{\rm jit,HIRES}$ (m s^{-1})	$0.51^{+0.47}_{-0.35}$	$3.68^{+0.31}_{-0.29}$	$2.84^{+0.29}_{-0.27}$	$2.81^{+0.29}_{-0.27}$	$0.63^{+0.51}_{-0.44}$	$0.55^{+0.47}_{-0.53}$	$\mathcal{U}(0, 10)$
$\sigma_{\rm jit,HARPS}$ (m s^{-1})	$0.67^{+0.46}_{-0.41}$	$2.44^{+0.50}_{-0.36}$	$1.68^{+0.42}_{-0.33}$	$1.66^{+0.38}_{-0.30}$	$0.83^{+0.48}_{-0.40}$	$1.30^{+0.31}_{-0.33}$	$\mathcal{U}(0, 10)$
$\sigma_{\rm jit,HARPS-N}$ (m s^{-1})	$1.44^{+0.29}_{-0.26}$	$2.93^{+0.31}_{-0.26}$	$2.07^{+0.25}_{-0.21}$	$2.09^{+0.24}_{-0.21}$	$1.04^{+0.23}_{-0.22}$	$1.14^{+0.34}_{-0.44}$	$\mathcal{U}(0, 10)$
$\sigma_{\rm jit,CARM}$ (m s^{-1})	...	$2.55^{+0.27}_{-0.27}$	$1.85^{+0.44}_{-0.32}$	$1.82^{+0.27}_{-0.26}$	$0.26^{+0.29}_{-0.17}$	$1.49^{+0.39}_{-0.47}$	$\mathcal{U}(0, 10)$
Hyper-parameters							
$K_{\rm QP,HIRES}$ (m s^{-1})	$3.16^{+0.44}_{-0.40}$	...	...	...	$3.24^{+0.50}_{-0.45}$	...	$\mathcal{U}(0.001, 10)$
$K_{\rm QP,HARPS}$ (m s^{-1})	$1.76^{+0.31}_{-0.28}$	...	...	...	$1.72^{+0.35}_{-0.28}$	...	$\mathcal{U}(0.001, 10)$
$K_{\rm QP,CARM}$ (m s^{-1})	...	...	...	...	$2.04^{+0.43}_{-0.34}$	...	$\mathcal{U}(0.001, 10)$
$\lambda_{\rm QP}$ (d)	23^{+31}_{-18}	...	...	...	49^{+14}_{-11}	...	$\mathcal{U}(5, 500)$
$w_{\rm QP}$	$0.48^{+0.31}_{-0.18}$	...	...	...	$0.50^{+0.14}_{-0.10}$	...	$\mathcal{U}(0, 1)$
$P_{\rm QP}$ (d)	$37.0^{+5.5}_{-14.6}$	...	...	...	$38.4^{+1.6}_{-1.3}$	...	$\mathcal{U}(20, 50)$
$\rm P_0$ (d)	...	...	...	...	...	$39.0^{+3.2}_{-4.3}$	$\mathcal{U}(1, 1500)$
τ (d)	...	...	...	...	...	820^{+923}_{-792}	$\mathcal{U}(1, 1500)$
$\rm S_0$	...	...	...	...	...	$0.48^{+0.96}_{-0.88}$	$\mathcal{U}(-15, 15)$
Fit quality							
$\sigma_{\rm O-C}$ (m s^{-1})	...	3.47	2.81	2.80	1.36	1.49	...
$\ln L$	...	−758.2	−691.9	−691.1	−637.7	−636.1	...
$\Delta \ln L$	...	0	66.3	67.1	120.5	122.1	...

once the main signal is removed, as shown in Fig. 8b, and there is also a signal at ∼37 d in the HARPS-N data just below the 0.1% FAP. Further subtracting the main signal of the residuals, the CARMENES dataset has a significant signal at ∼500 d, and two signals at the 1% level around 1100 and 120 d are seen in the combined dataset. These signals could be produced either by a long-term activity cycle or an offset mismatch between datasets, or by a long-period planet. After another iteration of subtraction, no other significant signals remain in the residuals.

Further, we searched for periodic signals in the GLS periodograms of the CARMENES activity indicators and photometric data. We investigated the possibility of the periodic RV variations being produced by stellar activity. As before, we consider a signal to be significant when it reaches a FAP below

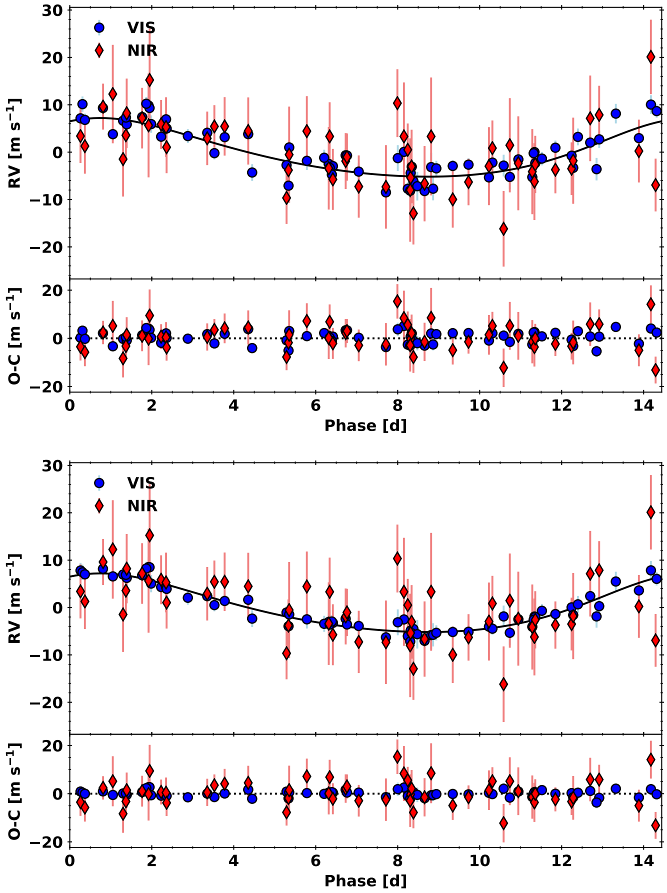

Fig. 6. LSPM J2116+0234 RVs of the CARMENES VIS and NIR channels phase-folded with the best Keplerian fit (*top*) and with the best Keplerian + GP fit (*bottom*), with a 14.441 d period.

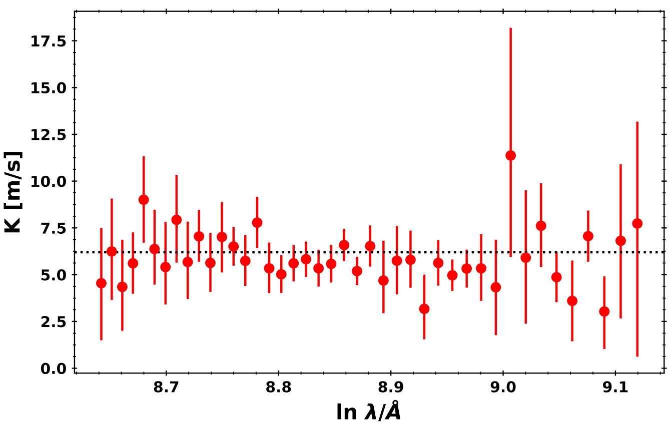

Fig. 7. Stability of the semi-amplitude of the signal as a function of the logarithm of the wavelength at the center on the order used for LSPM J2116+0234. The red circles show the semi-amplitudes of a Keplerian orbit fit using the velocities of each order individually. The values and uncertainties are computed from the MCMC posterior distribution. The black dashed line indicates the semi-amplitude found when using the combined RVs.

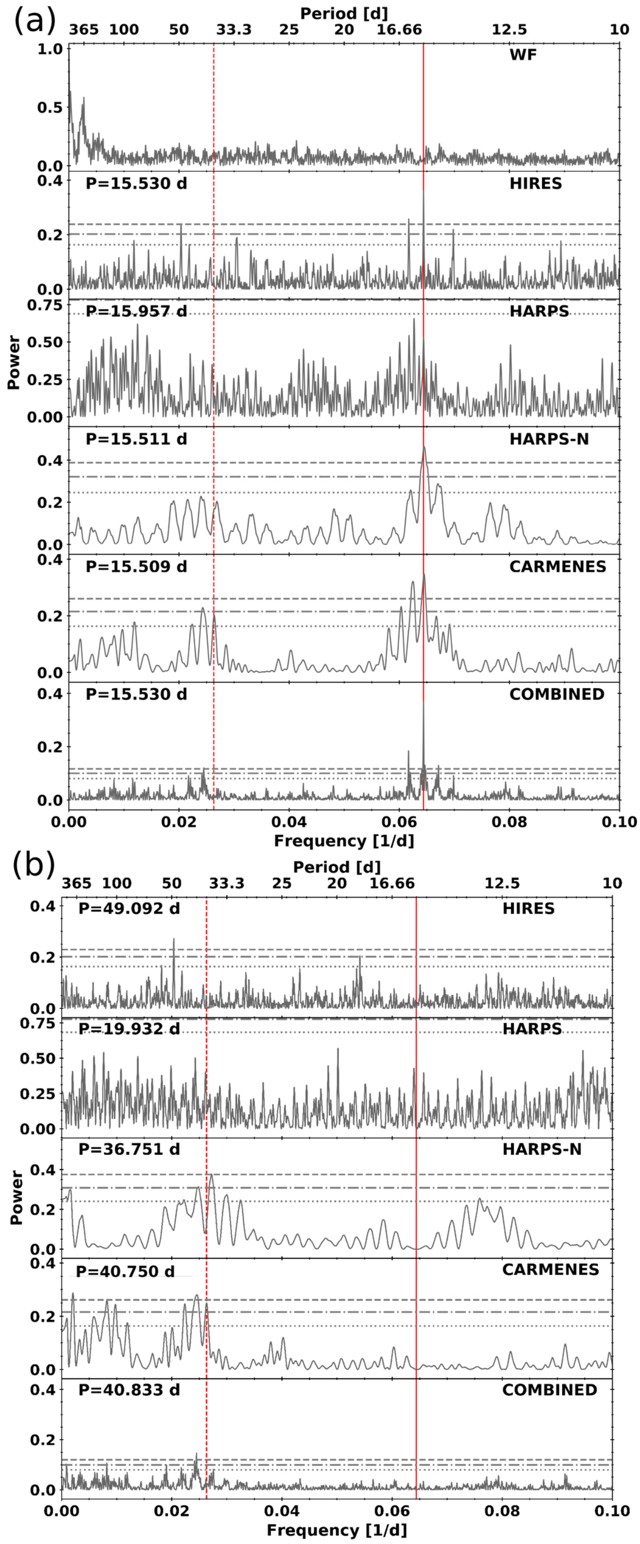

Fig. 8. (*a*) Generalized Lomb-Scargle periodograms of GJ 686 radial velocity data. The *top panel* shows the WF of the combined dataset. The next *four panels* represent the HIRES, HARPS, HARPS-N, and CARMENES data, respectively, and the *bottom panel* shows the periodogram of the combined dataset. The periods reported in each panel refer to the highest peak. Horizontal lines represent the bootstrapped FAP levels of 10, 1, and 0.1%. The vertical solid and dashed red lines indicate the period of the proposed planet and estimated stellar rotation period at 15.53 and ~38 d, respectively. (*b*) Generalized Lomb-Scargle periodograms of the RV residuals after removing a sinusoid with the period found in (a).

the 0.1% level. Figure 9 depicts the GLS periodograms of the dLW, CRX, the Hα, calcium infrared triplet (Ca IRT a, b and c), and sodium D doublet (Na D a and b) indices, and the contrast, FWHM, and bisector span of the CCFs, as introduced in

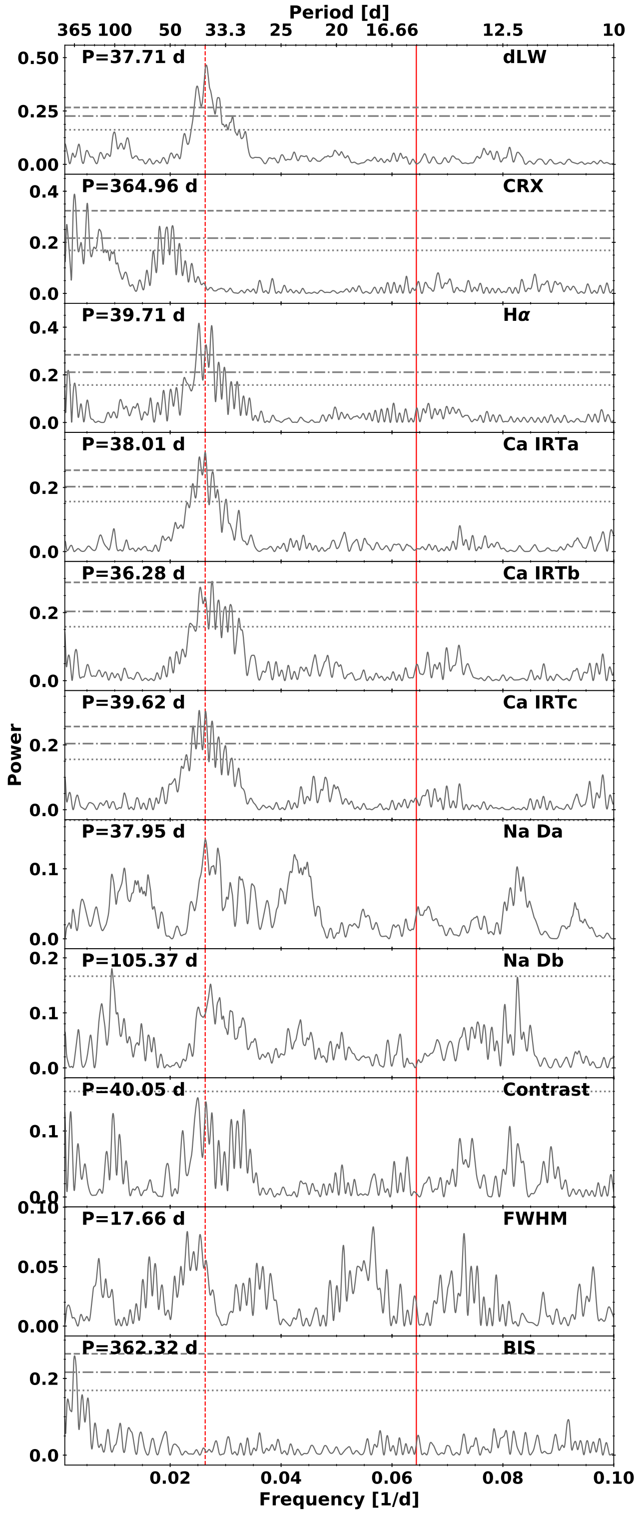

Fig. 9. Generalized Lomb-Scargle periodograms of the CARMENES activity indicators of GJ 686. The vertical solid line indicates the period of the suggested planet, while the vertical red dotted line denotes the period attributed to the rotation. The periods reported in each panel refer to the highest peak. Horizontal lines represent the bootstrapped 10, 1, and 0.1% FAP levels.

Sect. 3. There are several activity indicators with significant signals, among which there is a recurrence of signals between 36 and 40 d. However, neither of the activity indices show any significant signals at or near 15.53 d. The detected periods are in agreement with the periods found by Aff19 in the activity indicators. In particular, these authors found significant signals at 37 and 45 d in the Hα data from HARPS-N and HIRES, respectively, and a significant signal at 38 d in the S-index measured with HIRES. Furthermore, the activity time series during the last ~100 d of CARMENES observations also shows a modulation of the signals at ~38 d (see Fig. A.1 in the appendix). The modulation may be caused by an epoch of high stellar activity. Additionally, we also see significant signals in the CRX and BIS at 365 d caused by a combination of the WF and a long-period trend. The GLS periodograms of the residuals of the activity indicators (Fig. A.3, in the appendix), only show significant signals at long periods in Hα, and a signal just below the 1% FAP in the CRX. We further investigated the correlations between several activity indicators and the RV. As seen in Fig. A.7, we find significant correlations (p-values below 0.05) for a few activity indicators. This can be deduced by the strong modulations seen in Fig. A.1. We do not find correlations with the CRX or the Na I D lines, which might be only due to shifts in phase (Perger et al. 2019). Given that the signals at ~38 d are present in both RV and activity indicators, we attribute the variability to the stellar rotation period.

We plot the available photometric time series in Fig. 10, to investigate further the stellar rotation period. The GLS periodogram of the available photometry is depicted in Fig. 11. The MONET and ASAS photometry data show peaks at around 0.0279 d^{-1} (35.83 d) and 0.0264 d^{-1} (37.87 d). The V-band observations with SNO show a peak at ~45 d, although the broad amplitude of the peak makes it also compatible with the ~38 d signal observed in the activity indicators. However, the R-band observations with SNO and the V-band observations with LCO have peaks around 22 d. Since they do not have a counterpart in the RV activity indicators, the nature of these peaks is not clear. Finally, we note that the TJO R-band and LCO B-band photometry have signals around ~29 d, which may be caused by the lunar period. In fact, the S/N of the data is strongly modulated with a period of ~29 d, supporting this hypothesis. No other significant signals remain after the subtraction of this periodicity.

As a summary, based on the signals found in MONET and ASAS photometry and the activity indicators, we conclude that the rotation period of the star likely lies within the range 36–40 d. Further, we do not find any significant signal at ~15.53 d in the photometry and the activity indicators, and thus, this signal probably has a planetary origin.

4.2.1. Keplerian modeling

Assuming a planetary origin of the 15.5 day signal, we fit a Keplerian and a sinusoidal model to the combined RVs. We computed the orbital parameters and uncertainties using MCMC technique to infer the posterior distribution of the fitted parameters. The best-fit models and their uncertainties are shown in the fourth and fifth column of Table 5, respectively. We compared the $\Delta \ln L$ for both models, although the solutions were statistically equivalent ($\Delta \ln L < 1$). We adopted a circular model since $e \sin \omega$ and $e \cos \omega$ are consistent with zero within one sigma. The final parameters of the circular orbit give a planet with a period of 15.5311 ± 0.0015 d at $0.0917^{+0.0024}_{-0.0023}$ au, which produces an RV semi-amplitude of 2.83 ± 0.22 m s^{-1}. Using the stellar mass given in Table 1, we derive a minimum planet mass of $m_{\rm p} \sin i = 6.24^{+0.58}_{-0.59}\, M_{\oplus}$.

Using the derived orbital parameters, we investigated in detail all the accumulated photometric data for a possible planetary transit signature. The transit probability of GJ 686 b is

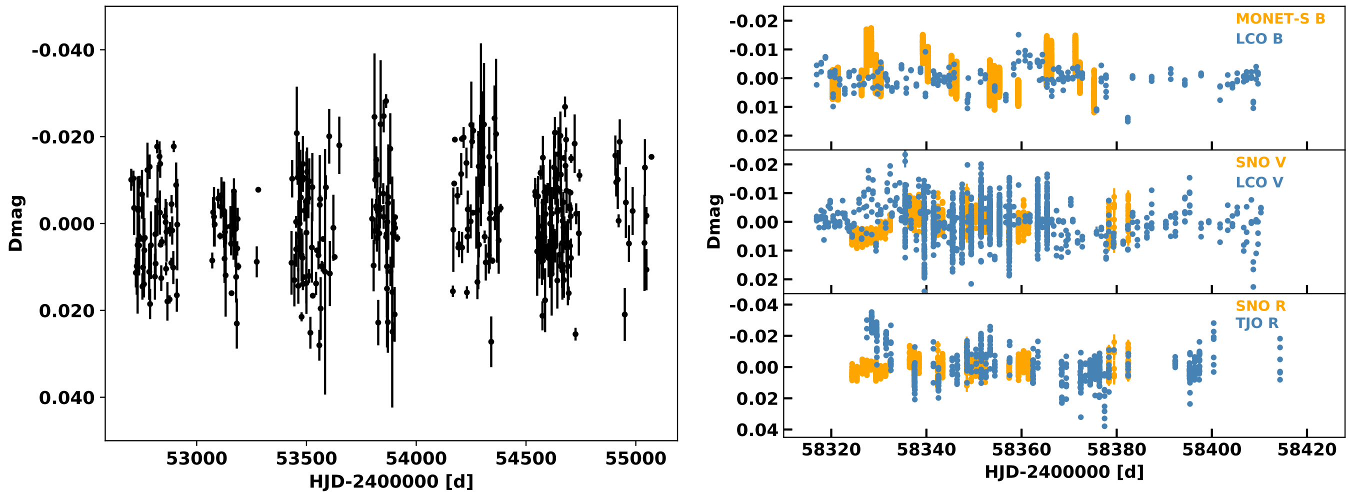

Fig. 10. *Left panel*: archival differential photometric data in *V* filter from ASAS. *Right panel*: differential photometric follow-up of GJ 686 in *B* filter with MONET-S and LCO (*top panel*), in *V* filter with SNO and LCO (*middle panel*) and in *R* filter with SNO and TJO (*bottom panel*).

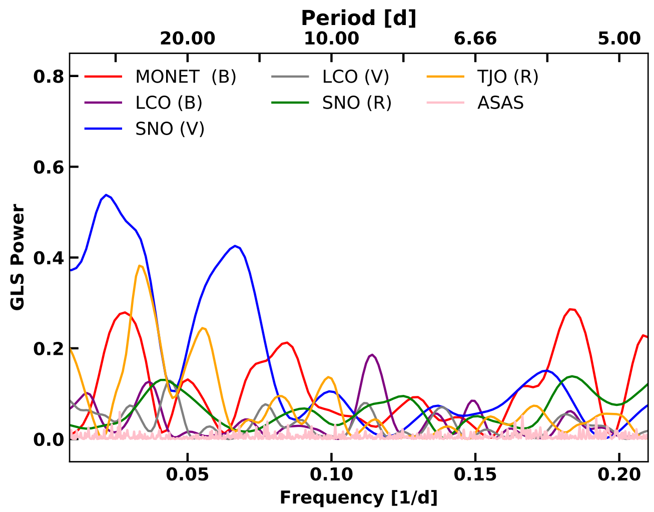

Fig. 11. Generalized Lomb-Scargle periodogram of all the photometric time series datasets of GJ 686.

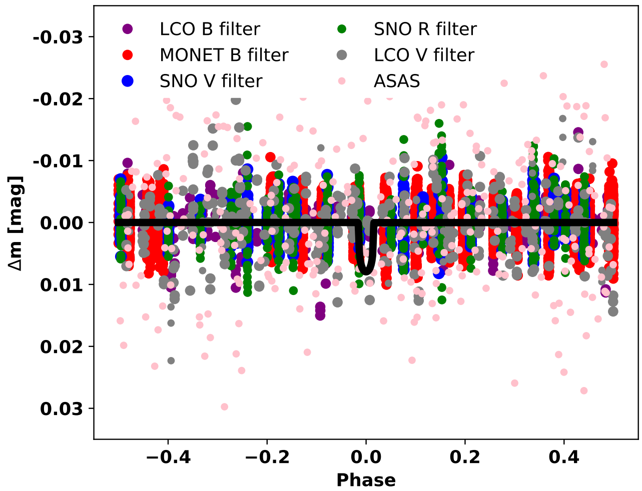

Fig. 12. Various photometric datasets phase-folded to 15.53 d, the orbital period of the planet. Depicted in black is the transit model showing the expected signal and maximum transit depth.

2.1%, and the transit duration would be 2.5 h. We detrended the photometric time series data and performed the box-fitting least squares (BLS) periodogram (Kovács et al. 2002). We find no significant signal. Furthermore, in Fig. 12 all photometric data phase-folded to the planetary period of 15.53 d along with an example of the expected transit signal. Since there are gaps in the photometric data, the estimated transit duration is ≈2.5 h and the uncertainties of the transit window are large.

4.2.2. Model comparison and signal stability

Using the same approach as for the previous system (see Sect. 4.1.2), we modeled our RV data with a null-model described by white noise, to evaluate the statistical significance of our models, and with a correlated-noise model that simultaneously fits the activity-induced RV variation and a Keplerian orbit.

The null model solution for GJ 686 is listed in the third column of Table 5. The best-fit null model yielded a $\ln L = -758.2$, which we used as a reference to compare the $\Delta \ln L$ against other models. For this star, the Δ lnL corresponding to a FAP of 1% and 0.1% are 13.4 and 17.4, respectively, as computed from a bootstrap randomization of 5000 permutations.

We modeled the planetary signal of GJ 686 and the activity term with a GP using a quasi-periodic function as the covariance matrix. Since HARPS and HARPS-N work in the same wavelength range, we modeled their RVs with the same amplitude K_{QP}. We list the parameter solution of this approach in the sixth column of Table 5. With a period of $15.5314^{+0.0015}_{-0.0014}$ d, the planetary signal has a RV semi-amplitude of $3.02^{+0.18}_{-0.20}$ m s^{-1}, which is slightly lower than the amplitude found in Aff19, but consistent within the uncertainties. Consequently, we also derive a smaller minimum mass of $6.64^{+0.53}_{-0.54}\,M_{\oplus}$. Unlike the model with only a planetary signal, in this case, we find a non-negligible eccentricity, of $0.077^{+0.056}_{-0.058}$, computed from $e \sin \omega$ and $e \cos \omega$. All the other orbital parameters are consistent within the respective uncertainties. We find a strong periodicity at $38.4^{+1.6}_{-1.3}$ d in the GP hyperparameters, reducing the uncertainties in Aff19 by about one order of magnitude. This periodicity is in agreement with the signals found in the activity indicators, therefore, we consider ~38.4 d as the rotation period of the star. Furthermore,

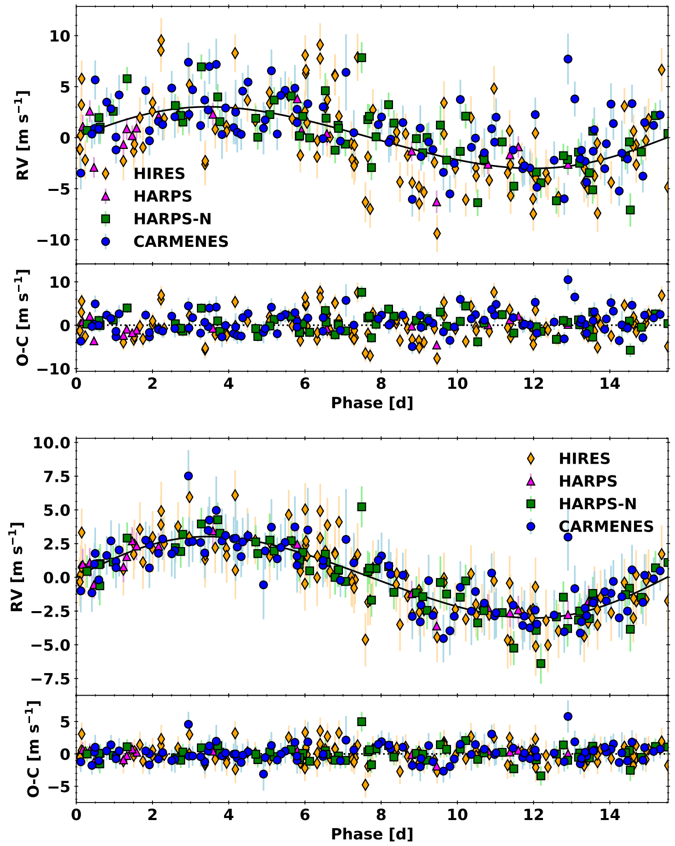

Fig. 13. Phase-folded RV measurements with HIRES, HARPS, HARPS-N, and CARMENES of GJ 686. *Top panel*: best-fit Keplerian model with a 15.531 d period. *Bottom panel*: best-fit Keplerian + GP model.

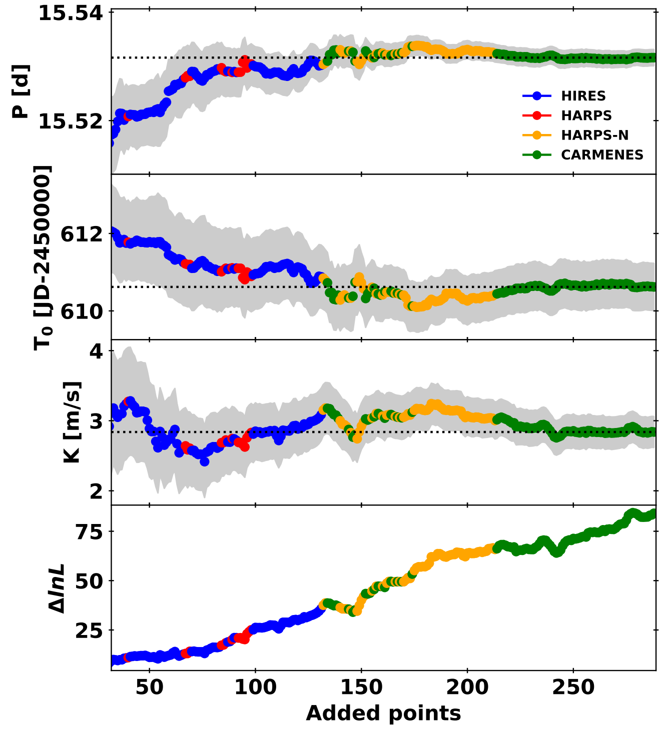

Fig. 14. Orbital parameters of a circular orbit and increment in the log likelihood as a function of the number of RV points, which are added chronologically. Each color represents a different instrument, and the gray shaded regions indicate the uncertainties computed from the MCMC posterior distribution. *First three panels*: period, time of maximum RV, and semi-amplitude, respectively. *Bottom panel*: increment in log likelihood with respect to a fit to the mean value. The black dotted line indicates the orbital parameters obtained from the combined RVs.

we find a large increase in $\ln L$ with respect to the null model and also with respect to the circular orbit model, with $\Delta \ln L$ of 120.5 and 53.4, respectively.

We show the phase-folded RV data for GJ 686 with the best Keplerian fit in Fig. 13 (top panel), while the best Keplerian + GP fit is depicted in the bottom panel. Figure A.5 shows the posterior distribution of the parameters and their correlations for GJ 686 with the planet + activity model. All the orbital parameters follow a well-behaved normal distribution and there are no strong correlations between parameters, except for the correlation between $e \sin \omega$ and $e \cos \omega$ with T_0.

Based on the orbital parameters obtained with the Keplerian plus activity model, we note a small decrease in the RV semi-amplitude of GJ 686 with respect to that found in Aff19, and further decrease when compared to the tentative signal found in Butler et al. (2017) of $3.46 \pm 0.56\,\mathrm{m\,s^{-1}}$. Although they are consistent within their respective uncertainties, the amplitudes of the signals are not directly comparable since Butler et al. (2017) have modeled only a Keplerian orbit, whereas Aff19 modeled a circular orbit plus an activity term and in this work we modeled a Keplerian + activity term. Hence, we checked the stability of the signal over time using the same model. We used a circular orbit, fixing the offsets and jitter terms to the values found in the fifth column of Table 5. We iteratively added the RV data in chronological order and computed the final parameters and uncertainties from the parameter distribution of an MCMC chain of 1000 steps. The results are shown in Fig. 14, with each color representing the instrument with which the RV measurement was made, and the gray shaded regions indicate the uncertainties. As observed, the amplitude is almost always compatible within uncertainties, and the period and time of periastron passage are stable after the addition of the 60th measurement.

Finally, we also modeled the tentative long-period signal found in the periodogram of residuals of the combined RV dataset after removing the planetary signal and the rotation period. We did that by simultaneously fitting two Keplerian orbits and an activity term modeled with a GP. We constrained the prior to periods longer than 100 d. This yielded a stable solution at a period of 1161^{+53}_{-81} d and a semi-amplitude of $1.44^{+0.44}_{-0.54}\,\mathrm{m\,s^{-1}}$, which would be produced by a planet of at least $13.4\,M_\oplus$ at 1.65 au. Nevertheless, adding a second planet is not statistically significant ($\Delta \ln L = 4.9$), and the signal could also be produced by the different offsets for each instrument or by a long-period activity cycle. Further observations are required to fully characterize this tentative long-period signal.

4.3. Exoplanets from CARMENES and habitability

According to Kopparapu et al. (2013), both stars have very similar habitable-zone locations that have optimistic inner limits at 0.13 and 0.14 au from the host stars LSPM J2116+0234 and GJ 686, respectively. The planets are closer to the host star than the conservative habitable-zone limits[6] of 0.16–0.32 au (Kopparapu et al. 2013). With semimajor axes of 0.087 au for the mini-Neptune around LSPM J2116+0234 and 0.092 au for the

[6] http://depts.washington.edu/naivpl/sites/default/files/hz.shtml

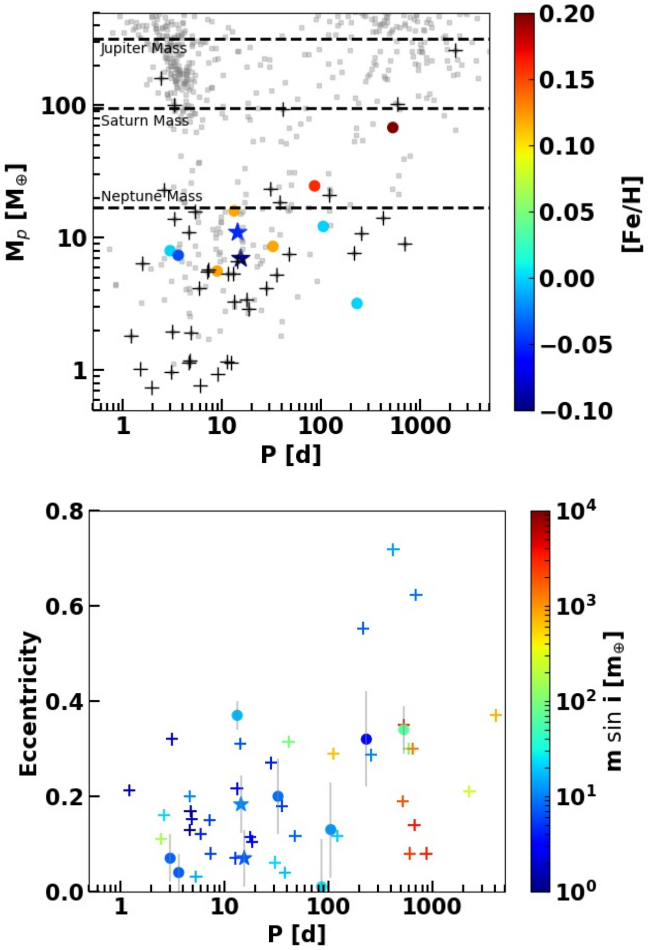

Fig. 15. *Top panel*: measured planetary masses from CARMENES against the planetary orbital periods are represented as color-coded circles using the stellar metallicity ([Fe/H]). The two planetary systems discussed in this paper are represented as stars. Other discoveries by CARMENES are depicted as circles. The scattered gray squares and black crosses are all known exoplanets[7] and planets orbiting M stars, respectively. The horizontal lines represent the mass of solar system planets. *Bottom panel*: eccentricity against the planetary orbital period of exoplanets around M stars (crosses). CARMENES planets are represented as circles and stars.

super-Earth around GJ 686, the two planets receive almost three times the flux received at the Earth by the Sun.

Both LSPM J2116+0234 b and GJ 686 b are in the lower part of the planetary mass versus orbital period diagram represented as star symbols in Fig. 15 (top panel). We also show the known exoplanets and the planets orbiting M dwarfs. This demonstrates the capability of CARMENES as an instrument to discover low-mass planets on both short and longer orbits around M dwarfs. Nearly ~75% of CARMENES discoveries are super-Earths or mini-Neptunes at a wide range of periods. We also note the lack of close-in massive planets around M stars. However, the two small planets reported in this paper with periods >10 d are part of a rather large population of planets with similar characteristic. The host stars of these planets have the lowest metallicity among the CARMENES discoveries. In Fig. 15 (bottom panel), we show the distribution of the eccentricity of M-dwarf exoplanets as a function of orbital period. The plot also shows the CARMENES discoveries including systems discussed in the current paper. We note that the majority of the super-Earths or mini-Neptunes have an eccentricity $e < 0.2$.

5. Summary

In this study, we analyze 72 and 57 RV measurements of the M3.0 V star LSPM J2116+0234 taken with the VIS and NIR channels of the high-resolution CARMENES échelle spectrograph, respectively. We also confirm and refine the orbital parameters of the super-Earth around the M1.0 V star GJ 686 reported in Affer et al. (2019) with the addition of 100 new RV CARMENES measurements.

The analysis of the RVs from LSPM J2116+0234 reveals a signal stable in wavelength at 14.44 d not present in activity indicators, which we interpret as being caused by a planet with a minimum mass of 13.3 $M_\oplus$ and a semimajor axis of 0.087 au.

To obtain better constraints on the properties of GJ 686 b derived in Affer et al. (2019), who used the available RVs from HIRES, HARPS and HARPS-N, we combine these data with the CARMENES-VIS RVs. We derive a slightly smaller and more precise RV semi-amplitude of 3.02 m s^{-1}, resulting in a lower minimum mass of the planet, of 6.64 $M_\oplus$. The orbital period of 15.5314 d and a semimajor axis of 0.092 au are very similar. Contrary to the best-fit model in Affer et al. (2019), our model suggests a non-zero eccentricity, obtaining a value of 0.077.

We use the photometric measurements and the activity indices to estimate of the rotation period of both LSPM J2116+0234 and GJ 686. For both targets, we adopt a nonparametric stellar variability model to account for correlated noise caused by stellar magnetic activity. We simultaneously model the stellar variability and the planetary signals to obtain a self-consistent planetary solution. From this model, we determine the stellar rotation period to be 42.0 d for LSPM J2116+0234 and 38.4 d for GJ 686. With the data currently available, the RV time series favor a single planet model for both LSPM J2116+0234 and GJ 686. However, an additional longer period signal may be present in the GJ 686 data, whose nature and properties need to be characterized with more measurements.

Acknowledgements. L.S. acknowledges support from the Deutsche Forschungsgemeinschaft under DFG DR 281/32-1. CARMENES is an instrument for the Centro Astronómico Hispano-Alemán de Calar Alto (CAHA, Almería, Spain). CARMENES is funded by the German Max-Planck-Gesellschaft (MPG), the Spanish Consejo Superior de Investigaciones Científicas (CSIC), the European Union through FEDER/ERF FICTS-2011-02 funds, and the members of the CARMENES Consortium (Max-Planck-Institut für Astronomie, Instituto de Astrofísica de Andalucía, Landessternwarte Königstuhl, Institut de Ciéncies de l'Espai, Insitut für Astrophysik Göttingen, Universidad Complutense de Madrid, Thüringer Landessternwarte Tautenburg, Instituto de Astrofísica de Canarias, Hamburger Sternwarte, Centro de Astrobiología and Centro Astronómico Hispano-Alemán), with additional contributions by the Spanish Ministry of Economy, the German Science Foundation through the Major Research Instrumentation Programme and DFG Research Unit FOR2544 "Blue Planets around Red Stars", the Klaus Tschira Stiftung, the states of Baden-Württemberg and Niedersachsen, and by the Junta de Andalucía. Data were partly obtained with the MONET/South telescope of the MOnitoring NEtwork of Telescopes, funded by the Alfried Krupp von Bohlen und Halbach Foundation, Essen, and operated by the Georg-August-Universität Göttingen, the McDonald Observatory of the University of Texas at Austin, and the South African Astronomical Observatory. Data were partly collected with the 90 cm telescope at Sierra Nevada Observatory (SNO) operated by the Instituto de Astrofíífica de Andalucía (IAA). We acknowledge financial support from the Spanish Ministry for Science, Innovation and Universities (MCIU) AYA2015-69350-C3-2-P, ESP2016-80435-C2-1-R, ESP2016-80435-C2-2-R, AYA2016-79425-C3-1/2/3-P, ESP2017-87676-C05-02-R, ESP2017-87143-R, BES-2017-082610, SEV-2015-0548-17-2, Generalitat de Catalunya/CERCA programme; Agència de Gestió d'Ajuts Universitaris i de Recerca of the Generalitat de Catalunya through grant 2018FI_B_00188, and the Israel Science Foundation through grant 848/16. This work makes use

[7] http://exoplanets.org

of data from the HARPS-N Project, a collaboration between the Astronomical Observatory of the Geneva University (lead), the CfA in Cambridge, the Universities of St. Andrews and Edinburgh, the Queens University of Belfast, and the TNG-INAF Observatory; from observations obtained at the W. M. Keck Observatory, which is operated as a scientific partnership among the California Institute of Technology, the University of California and the National Aeronautics and Space Administration. The Observatory was made possible by the generous financial support of the W. M. Keck Foundation; from observations collected at the European Organisation for Astronomical Research in the Southern Hemisphere under ESO programmes 183.C-0437(A) and 072.C-0488(E); from the European Space Agency (ESA) mission *Gaia* (`https://www.cosmos.esa.int/gaia`), processed by the *Gaia* Data Processing and Analysis Consortium (DPAC, `https://www.cosmos.esa.int/web/gaia/dpac/consortium`). Funding for the DPAC has been provided by national institutions, in particular the institutions participating in the *Gaia* Multilateral Agreement.

References

Adams, W. S., Joy, A. H., & Humason, M. L. 1926, ApJ, 64, 225
Affer, L., Damasso, M., Micela, G., et al. 2019, A&A, 622, A193
Alonso-Floriano, F. J., Morales, J. C., Caballero, J. A., et al. 2015, A&A, 577, A128
Ambikasaran, S., Foreman-Mackey, D., Greengard, L., Hogg, D. W., & O'Neil, M. 2015, IEEE Trans. Pattern. Anal. Mach. Intell., 38, 252
Anglada-Escudé, G., & Butler, R. P. 2012, ApJS, 200, 15
Angus, R., Morton, T., Aigrain, S., Foreman-Mackey, D., & Rajpaul, V. 2018, MNRAS, 474, 2094
Baluev, R. V. 2009, MNRAS, 393, 969
Baluev, R. V. 2013, Astron. Comput., 2, 18
Barnard, E. E. 1913, ApJ, 38, 496
Barnes, S. A. 2007, ApJ, 669, 1167
Barnes, J. R., Jeffers, S. V., & Jones, H. R. A. 2011, MNRAS, 412, 1599
Barrado y Navascués, D., Stauffer, J. R., & Jayawardhana, R. 2004, ApJ, 614, 386
Bauer, F. F., Zechmeister, M., & Reiners, A. 2015, A&A, 581, A117
Boisse, I., Bouchy, F., Hébrard, G., et al. 2011, in Physics of Sun and Star Spots, eds. D. Prasad Choudhary, & K. G. Strassmeier, IAU Symp., 273, 281
Bonfils, X., Delfosse, X., Udry, S., et al. 2013, A&A, 549, A109
Butler, R. P., Vogt, S. S., Laughlin, G., et al. 2017, AJ, 153, 208
Caballero, J. A., Guàrdia, J., López del Fresno, M., et al. 2016, in Observatory Operations: Strategies, Processes, and Systems VI, Proc. SPIE, 9910, 99100E
Cortés-Contreras, M. 2016, PhD Thesis, Universidad Complutense de Madrid, Spain
Dahm, S. E. 2015, ApJ, 813, 108
Delfosse, X., Forveille, T., Perrier, C., & Mayor, M. 1998, A&A, 331, 581
Desort, M., Lagrange, A.-M., Galland, F., Udry, S., & Mayor, M. 2007, A&A, 473, 983
Díez Alonso, E., Caballero, J. A., Montes, D., et al. 2019, A&A, 621, A126
Drake, A. J., Djorgovski, S. G., Mahabal, A., et al. 2009, ApJ, 696, 870
Dressing, C. D., & Charbonneau, D. 2015, ApJ, 807, 45
Dumusque, X. 2018, A&A, 620, A47
Eggen, O. J. 1995, AJ, 110, 2862
Faria, J. P., Haywood, R. D., Brewer, B. J., et al. 2016, A&A, 588, A31
Finch, C. T., & Zacharias, N. 2016, AJ, 151, 160
Finch, C. T., Zacharias, N., Subasavage, J. P., Henry, T. J., & Riedel, A. R. 2014, AJ, 148, 119
Foreman-Mackey, D., Hogg, D. W., Lang, D., & Goodman, J. 2013, PASP, 125, 306
Foreman-Mackey, D., Agol, E., Angus, R., & Ambikasaran, S. 2017, AJ, 154, 220
Frith, J., Pinfield, D. J., Jones, H. R. A., et al. 2013, MNRAS, 435, 2161
Gaia Collaboration (Prusti, T., et al.) 2016, A&A, 595, A1
Gaia Collaboration (Brown, A. G. A., et al.) 2018, A&A, 616, A1
Gaidos, E., Mann, A. W., Lépine, S., et al. 2014, MNRAS, 443, 2561
Gaidos, E., Mann, A. W., Kraus, A. L., & Ireland, M. 2016, MNRAS, 457, 2877
Hawley, S. L., Gizis, J. E., & Reid, I. N. 1996, AJ, 112, 2799
Haywood, R. D., Collier Cameron, A., Queloz, D., et al. 2014, MNRAS, 443, 2517
Henry, T. J., Kirkpatrick, J. D., & Simons, D. A. 1994, AJ, 108, 1437
Henry, T. J., Jao, W.-C., Subasavage, J. P., et al. 2006, AJ, 132, 2360
Herbst, W., & Layden, A. C. 1987, AJ, 94, 150
Husser, T.-O., Wende-von Berg, S., Dreizler, S., et al. 2013, A&A, 553, A6
Isaacson, H., & Fischer, D. 2010, ApJ, 725, 875
Jeffers, S. V., Barnes, J. R., Jones, H. R. A., et al. 2014, MNRAS, 438, 2717
Jeffers, S. V., Schöfer, P., Lamert, A., et al. 2018, A&A, 614, A76
Jones, D. E., Stenning, D. C., Ford, E. B., et al. 2017, ArXiv e-prints [arXiv:1711.01318]
Kaminski, A., Trifonov, T., Caballero, J. A., et al. 2018, A&A, 618, A115
Koen, C., Kilkenny, D., van Wyk, F., & Marang, F. 2010, MNRAS, 403, 1949
Kopparapu, R. K., Ramirez, R., Kasting, J. F., et al. 2013, ApJ, 765, 131
Kovács, G., Zucker, S., & Mazeh, T. 2002, A&A, 391, 369
Lépine, S., & Shara, M. M. 2005, AJ, 129, 1483
Lépine, S., & Gaidos, E. 2011, AJ, 142, 138
Lépine, S., Hilton, E. J., Mann, A. W., et al. 2013, AJ, 145, 102
Luque, R., Nowak, G., Pallé, E., et al. 2018, A&A, 620, A171
Marcy, G. W., & Butler, R. P. 1998, ARA&A, 36, 57
Mayor, M., & Queloz, D. 1995, Nature, 378, 355
McCully, C., Volgenau, N. H., Harbeck, D.-R., et al. 2018, in Software and Cyberinfrastructure for Astronomy V, SPIE Conf. Ser., 10707, 107070K
Montes, D., López-Santiago, J., Gálvez, M. C., et al. 2001, MNRAS, 328, 45
Mortier, A., Bonomo, A. S., Rajpaul, V. M., et al. 2018, MNRAS, 481, 1839
Nagel, E., Czesla, S., Schmitt, J. H. M. M., et al. 2019, A&A, 622, A153
Newton, I. 1687, Philosophiae naturalis principia mathematica (London: J. Societatis Regiae ac Typis J. Streater)
Newton, E. R., Irwin, J., Charbonneau, D., et al. 2017, ApJ, 834, 85
Oshagh, M., Santos, N. C., Figueira, P., et al. 2017, A&A, 606, A107
Osvalds, V. 1957, AJ, 62, 274
Panagi, P. M., & Mathioudakis, M. 1993, A&AS, 100, 343
Passegger, V. M., Reiners, A., Jeffers, S. V., et al. 2018, A&A, 615, A6
Patten, B. M., & Simon, T. 1996, ApJS, 106, 489
Perger, M., Scandariato, G., Ribas, I., et al. 2019, A&A, 624, A123
Pojmański, G. 1997, Acta Astron., 47, 467
Queloz, D., Henry, G. W., Sivan, J. P., et al. 2001, A&A, 379, 279
Quirrenbach, A., Amado, P. J., Caballero, J. A., et al. 2014, in Ground-based and Airborne Instrumentation for Astronomy V, Proc. SPIE, 9147, 91471F
Quirrenbach, A., Amado, P. J., Caballero, J. A., et al. 2016, in Ground-based and Airborne Instrumentation for Astronomy VI, Proc. SPIE, 9908, 990812
Quirrenbach, A., Amado, P. J., Ribas, I., et al. 2018, in Ground-based and Airborne Instrumentation for Astronomy VII, SPIE Conf. Ser., 10702, 107020W
Rajpaul, V., Aigrain, S., Osborne, M. A., Reece, S., & Roberts, S. 2015, MNRAS, 452, 2269
Rasmussen, C. E., & Williams, C. K. I. 2005, Gaussian Processes for Machine Learning (Adaptive Computation and Machine Learning) (Cambridge: MIT Press)
Rebull, L. M., Stauffer, J. R., Bouvier, J., et al. 2016, AJ, 152, 113
Reiners, A., Bean, J. L., Huber, K. F., et al. 2010, ApJ, 710, 432
Reiners, A., Shulyak, D., Anglada-Escudé, G., et al. 2013, A&A, 552, A103
Reiners, A., Ribas, I., Zechmeister, M., et al. 2018a, A&A, 609, L5
Reiners, A., Zechmeister, M., Caballero, J. A., et al. 2018b, A&A, 612, A49
Ribas, I., Tuomi, M., Reiners, A., et al. 2018, Nature, 563, 365
Rodríguez, E., García, J. M., Costa, V., et al. 2010, MNRAS, 408, 2149
Rutten, R. G. M., Schrijver, C. J., Zwaan, C., Duncan, D. K., & Mewe, R. 1989, A&A, 219, 239
Sarkis, P., Henning, T., Kürster, M., et al. 2018, AJ, 155, 257
Schäfer, S., Guenther, E. W., Reiners, A., et al. 2018, in Ground-based and Airborne Instrumentation for Astronomy VII, SPIE Conf. Ser., 10702, 1070276
Schönfeld, E. 1886, Bonner Durchmusterung des sudlichen Himmels (Bonn: Eds Marcus and Weber's Verlag)
Schweitzer, A., Passegger, V. M., Cifuentes, C., et al. 2019, A&A, 625, A68
Skrutskie, M. F., Cutri, R. M., Stiening, R., et al. 2006, AJ, 131, 1163
Stauffer, J. R., & Hartmann, L. W. 1986, ApJS, 61, 531
Stephenson, C. B. 1986, AJ, 92, 139
Suárez Mascareño, A., Rebolo, R., González Hernández, J. I., et al. 2018, A&A, 612, A89
Tal-Or, L., Trifonov, T., Zucker, S., Mazeh, T., & Zechmeister, M. 2019, MNRAS, 484, L8
Tokovinin, A. A. 1990, Pisma v Astronomicheskii Zhurnal, 16, 52
Trifonov, T., Kürster, M., Zechmeister, M., et al. 2018, A&A, 609, A117
Udry, S., Bonfils, X., Delfosse, X., et al. 2007, A&A, 469, L43
Vogt, S. S., & Penrod, G. D. 1983, PASP, 95, 565
Wilson, R. E. 1953, General Catalogue of Stellar Radial Velocities (Washington D.C.: Carnegie Institute of Washington Publication)
Wright, J. T., Marcy, G. W., Butler, R. P., & Vogt, S. S. 2004, ApJS, 152, 261
Zacharias, N., Finch, C. T., Girard, T. M., et al. 2013, AJ, 145, 44
Zechmeister, M., & Kürster, M. 2009, A&A, 496, 577
Zechmeister, M., Reiners, A., Amado, P. J., et al. 2018, A&A, 609, A12

[1] Institut für Astrophysik, Georg-August-Universität, Friedrich-Hund-Platz 1, 37077 Göttingen, Germany
e-mail: `lalitha.sairam@uni-goettingen.de`

[2] Institut de Ciències de l'Espai (ICE, CSIC), Campus UAB, C/ de Can Magrans s/n, 08193 Bellaterra (Cerdanyola del Vallès), Barcelona, Spain
[3] Institut d'Estudis Espacials de Catalunya (IEEC), C/ Gran Capità 2-4, 08034 Barcelona, Spain
[4] Hamburger Sternwarte, Gojenbergsweg 112, 21029 Hamburg, Germany
[5] Instituto de Astrofísica de Andalucía (IAA-CSIC), Glorieta de la Astronomía s/n, 18008 Granada, Spain
[6] Instituto de Astrofísica de Canarias, Vía Láctea s/n, 38205 La Laguna, Tenerife, Spain
[7] Departamento de Astrofísica, Universidad de La Laguna, 38026 La Laguna, Tenerife, Spain
[8] Centro de Astrobiología (CSIC-INTA), ESAC, Camino Bajo del Castillo s/n, 28692 Villanueva de la Cañada, Madrid, Spain
[9] Landessternwarte, Zentrum für Astronomie der Universtät Heidelberg, Königstuhl 12, 69117 Heidelberg, Germany
[10] Centro Astronónomico Hispano Alemán, Observatorio de Calar Alto, Sierra de los Filabres, 04550 Gergal, Spain
[11] Thüringer Landesstenwarte Tautenburg, Sternwarte 5, 07778 Tautenburg, Germany
[12] Max-Planck-Institut für Astronomie, Königstuhl 17, 69117 Heidelberg, Germany
[13] Departamento de Física de la Tierra y Astrofísica and IPARCOS-UCM (Intituto de Física de Partículas y del Cosmos de la UCM), Facultad de Ciencias Físicas, Universidad Complutense de Madrid, 28040 Madrid, Spain
[14] Department of Geophyics, Raymond and Beverly Sackler Faculty of Exact Sciences, Tel Aviv University, Tel Aviv 6997801, Israel

Appendix A: Additional periodograms, data table, and MCMC posterior distributions

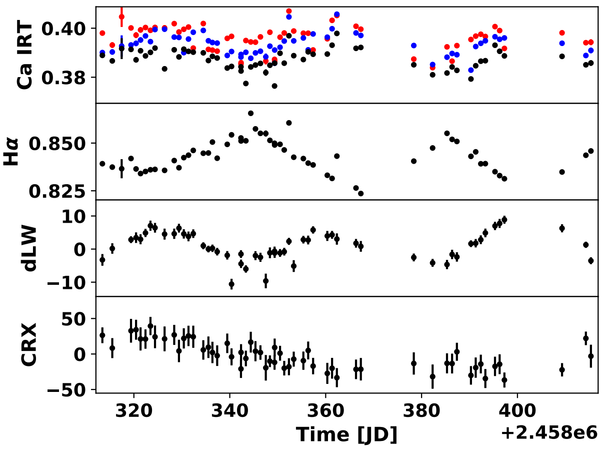

Fig. A.1. Time series of activity indicators, dLW, and CRX for the last 100 days of observations of GJ 686.

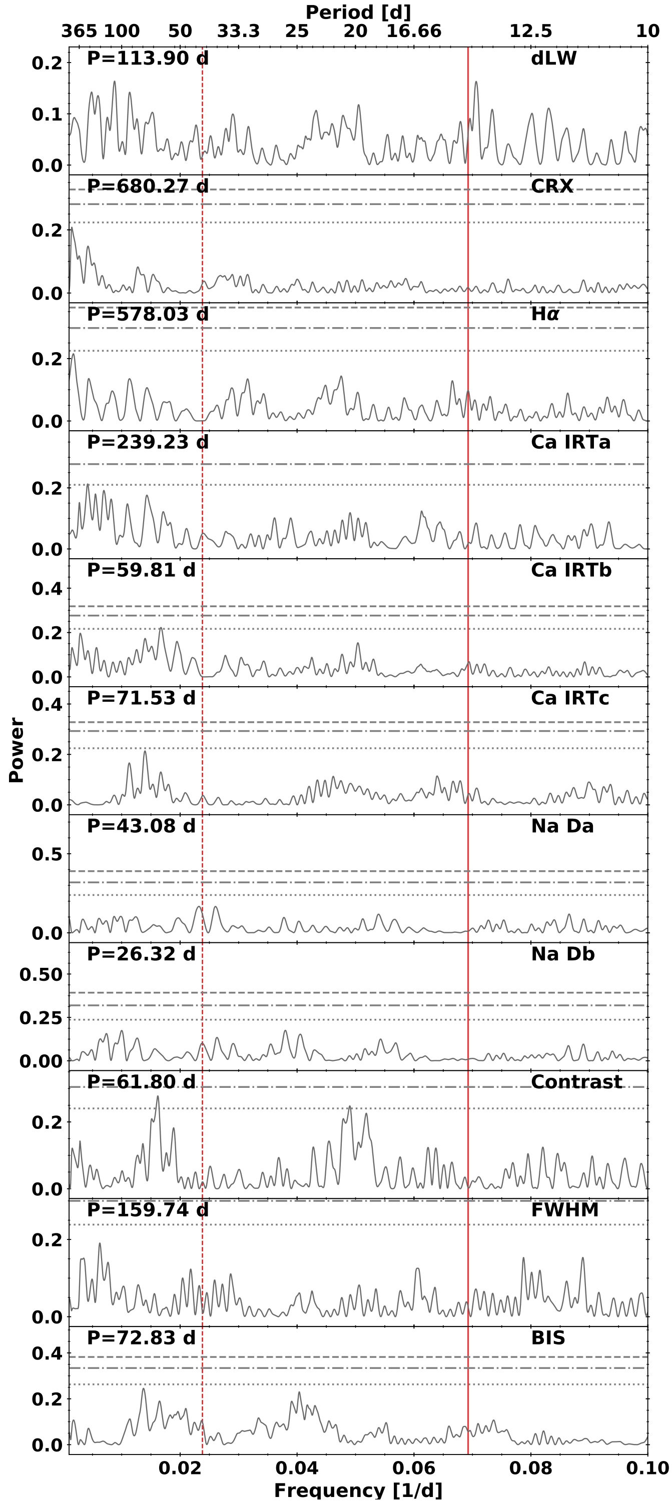

Fig. A.2. Periodograms of the residuals after subtracting the highest signal of the activity indicators of LSPM J2116+0234. The vertical solid line indicates the period of the suggested planet, while the vertical red dotted line denotes the period attributed to the rotation period. The periods reported in each panel refer to the highest peak. The horizontal lines represent the bootstrapped 10, 1, and 0.1% FAP levels.

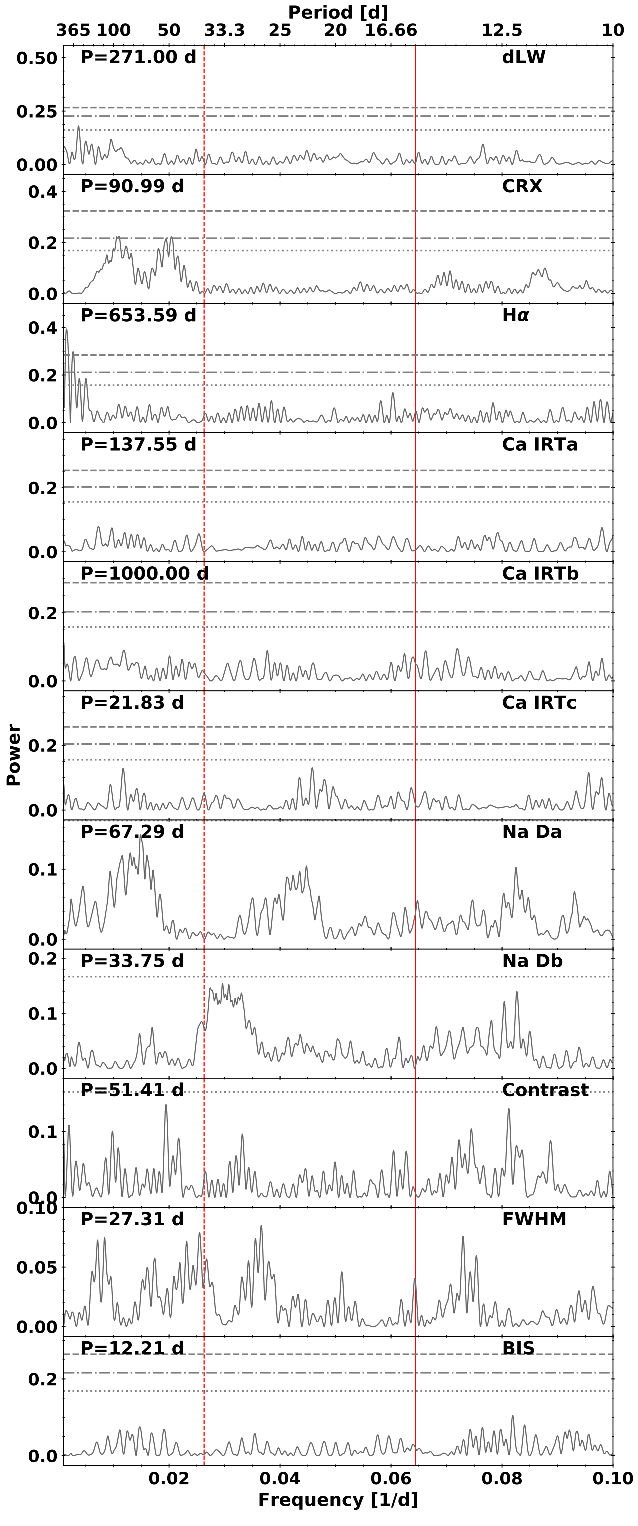

Fig. A.3. Periodograms of the residuals after subtracting the highest signal of the activity indicators of GJ 686. The vertical solid line indicates the period of the suggested planet, while the vertical red dotted line denotes the period attributed to the rotation period. The periods reported in each panel refer to the highest peak. The horizontal lines represent the bootstrapped 10, 1, and 0.1% FAP levels.

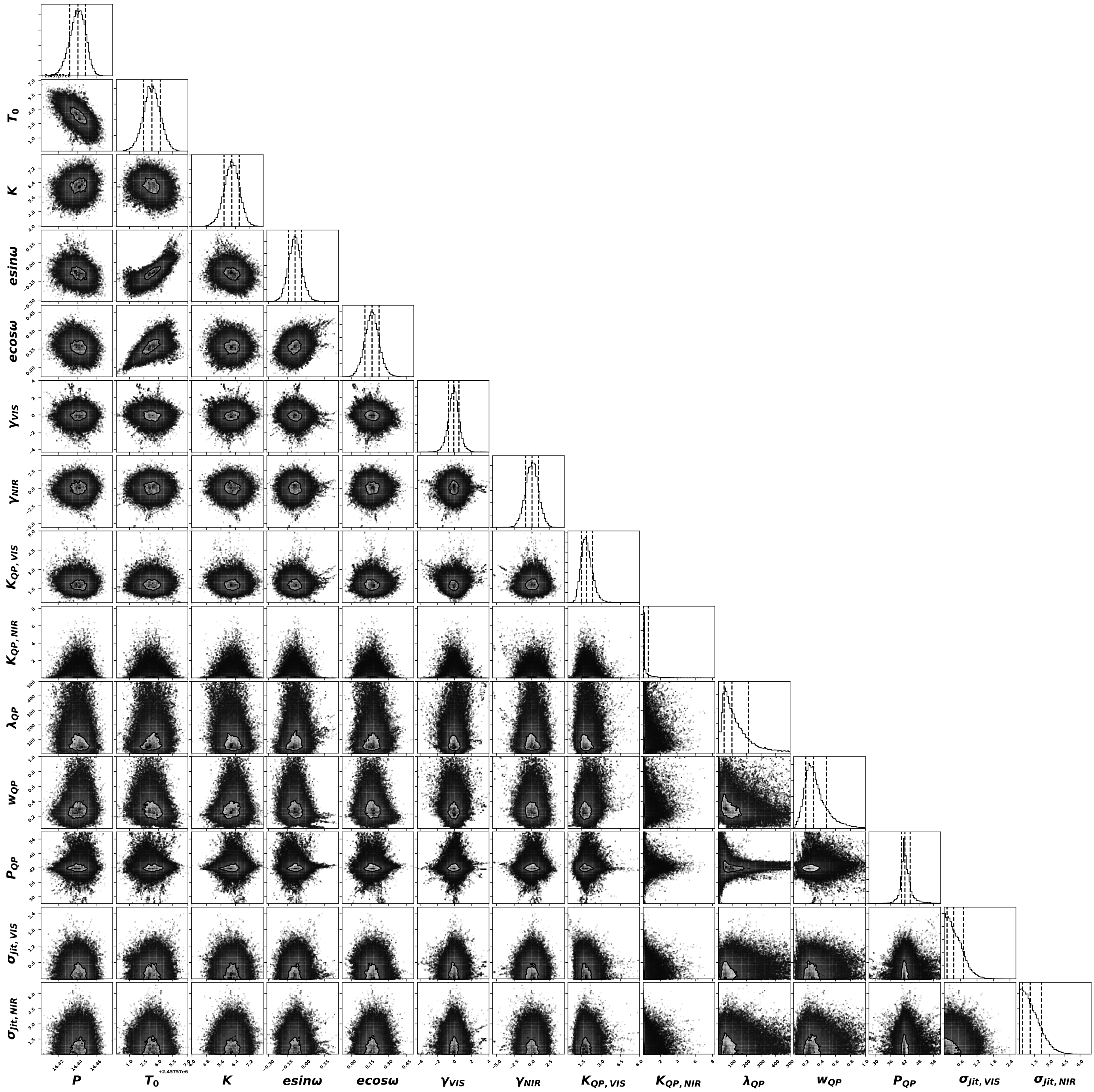

Fig. A.4. Posterior distributions from the MCMC analysis on LSPM J2116+0234 b. Plotted are the planetary parameters, instrumental offsets ($\gamma_{\rm VIS}$, $\gamma_{\rm NIR}$), GP hyper-parameters ($K_{\rm QP}$, $\lambda_{\rm QP}$, $w_{\rm QP}$, $P_{\rm QP}$), and additional data jitters ($\sigma_{\rm Jit,VIS}$, $\sigma_{\rm Jit,NIR}$). The vertical dashed lines indicate the mean and 1σ uncertainties of the fitted parameters.

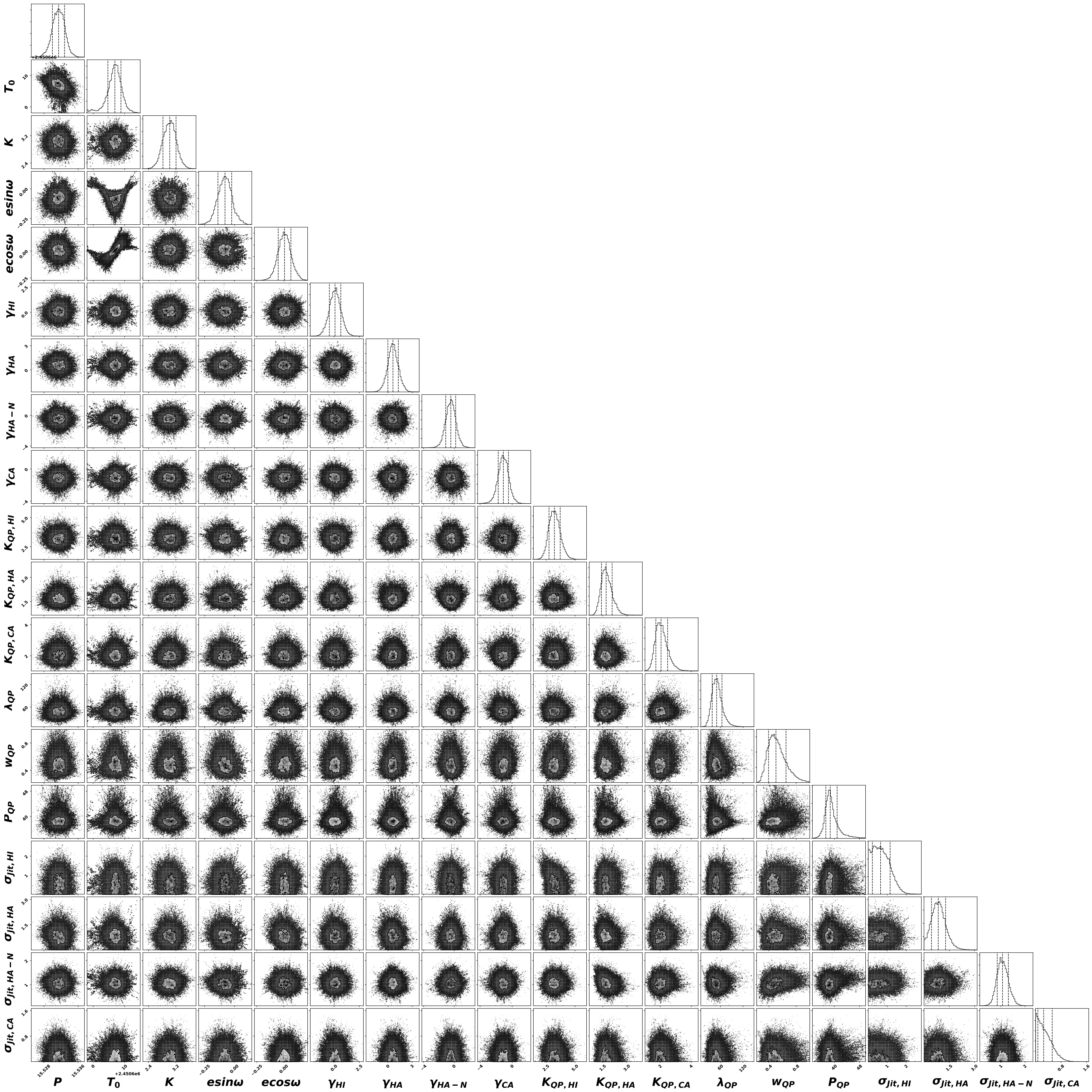

Fig. A.5. Posterior distributions from the MCMC analysis on GJ 686 b. Plotted are the planetary parameters, instrumental offsets ($\gamma_{\rm HIRES}$, $\gamma_{\rm HARPS}$, $\gamma_{\rm HARPS-N}$, $\gamma_{\rm CARMENES}$), GP hyper-parameters ($K_{\rm QP}$, $\lambda_{\rm QP}$, $w_{\rm QP}$, $P_{\rm QP}$), and additional data jitters ($\sigma_{\rm Jit,HIRES}$, $\sigma_{\rm Jit,HARPS}$, $\sigma_{\rm Jit,HARPS-N}$, $\sigma_{\rm Jit,CARMENES}$). The vertical dashed lines indicate the mean and 1σ uncertainties of the fitted parameters.

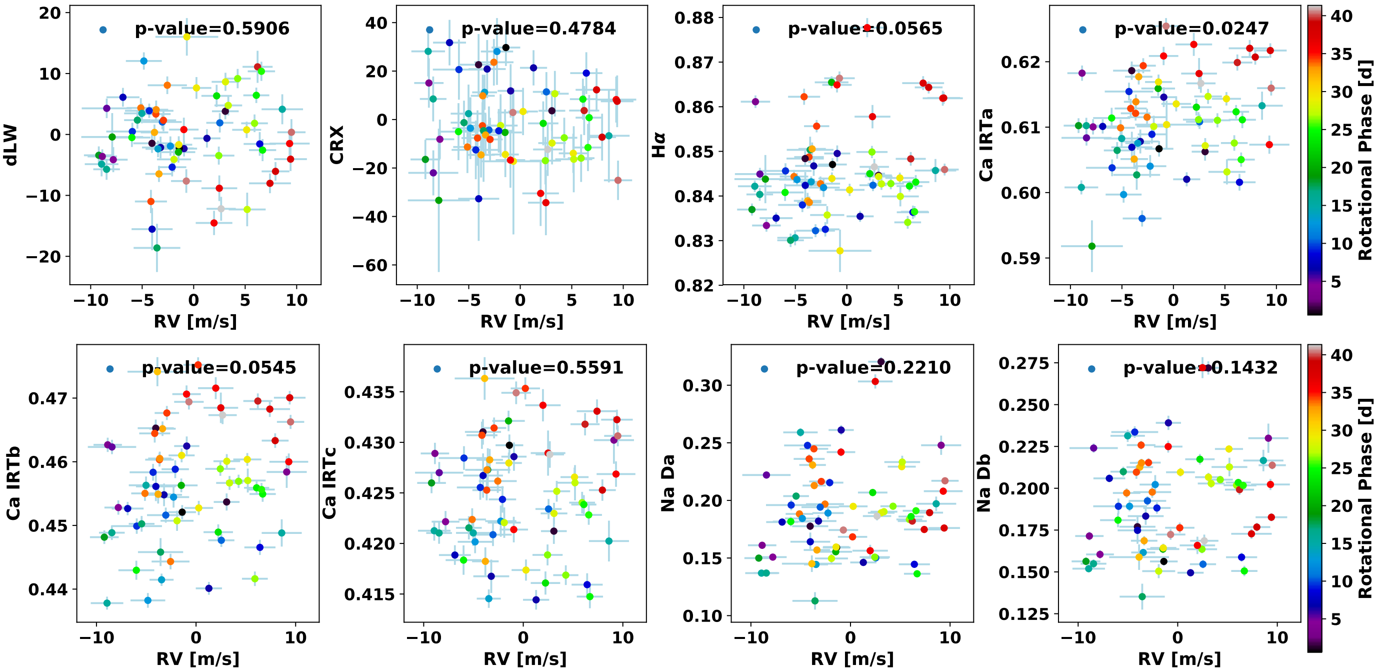

Fig. A.6. Correlation plots between the activity indices and radial velocities of LSPM J2116+0234. Color code represents the phase with the estimated rotation period of 42 d. The *p*-value of a linear fit is shown.

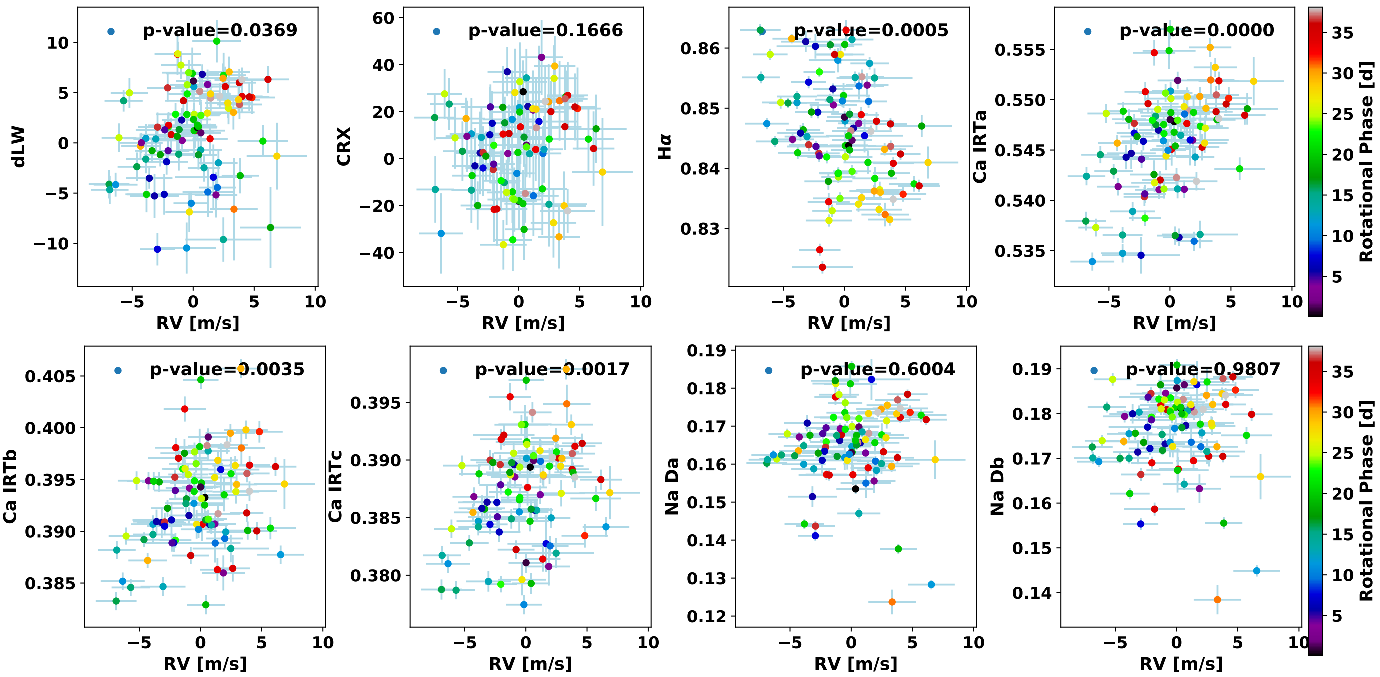

Fig. A.7. *Top panels*: correlation plots between the activity indices and radial velocities of GJ 686. Color code represents the phase with the estimated rotation period of 38.4 d. The *p*-value of a linear fit is shown.